The Role of Photoinduced Charge Transfer for Photocatalysis, Photoelectrocatalysis and Luminescent Sensing in Metal-Organic Frameworks

ARTICLE

The Role of Photoinduced Charge Transfer for Photocatalysis, Photoelectrocatalysis and Luminescent Sensing in Metal–Organic Frameworks

Xinlin Li, Sreehari Surendran, Jierui Yu, and Pravas Deria*

Metal–organic frameworks (MOFs) have emerged as promising porous optoelectronic compositions for energy conversion and sensing applications. The enormous structural possibilities, the large variety of photo- and redox-active building blocks along with several post-synthetic functionalization strategies make MOFs an ideal platform for photochemical and photoelectrochemical developments. Because MOFs assemble all the active building units in dense fashion, the non-aggregated yet proximally positioned species ensure the efficient photon absorption to drive photoinduced charge transfer (PCT) reactions for energy conversion and sensing. Hence, understanding the PCT processes within MOFs as a function of its topological and electronic structure of donor-acceptor (D-A) moieties can provide transformative strategies to design new low-density compositions.

Introduction

Metal–organic frameworks (MOFs) are an emerging class of porous compositions with modular topology and pore structure defining their desired properties.[1-5] These frameworks are commonly constructed by interconnecting metal-ion based secondary building units (SBUs) or nodes through organic linkers or struts and the resulting porous compositions were originally projected as next-generation materials for separation and storage.[6-11] Over the years, these framework compositions have shown promising applications in photovoltaics,[12-14] photocatalysis,[15-21] and fluorescent sensors depending on the electronic properties of the components.[22-27] The enormous structural diversity, the molecular-scale porosity (for reactant/analyte delivery and product release), and the comparative ease of integration with redox-catalysts have made MOFs an attractive platform for photophysical and photochemical developments. The reticular framework chemistry has shown that linkers with similar molecular backbone can be assembled in identical topological networks - thus allowing the route for electronic tuning. Besides the flexible choices of linkers, MOFs can be post-synthetically functionalized[28-30] *via*, for example, linker modification,[28, 31] metal or linker exchange,[32, 33] or solvent-assisted ligand incorporation (SALI)[34-36] to integrate complementary functional chromophores or redox moieties with appropriate electronic properties and energies for the desired photoinduced processes.

Department of Chemistry and Biochemistry, Southern Illinois University, 1245 Lincoln Drive, Carbondale, Illinois 62901, United States
† Footnotes relating to the title and/or authors should appear here.
Electronic Supplementary Information (ESI) available: [details of any supplementary information available should be included here]. See DOI: 10.1039/x0xx00000x

MOFs can be prepared both as crystalline and amorphous variants, however, the former is the most studied form due to its precise and periodic positioning of the building units that makes the understanding of the structure-property correlation easier. The key feature of these 3D solid porous frameworks is their ability to densely assemble chromophoric linkers (in hundreds of millimolar) around the pores. This ensures high photon absorptivity and provides a way to circumvent the extant challenges stemming from various unproductive exciton recombination processes observed in common molecular aggregates. Thus, the dense arrangement of chromophores in MOFs can constitute a near-ideal system for photocatalysis. For photoelectrocatalysis, MOF-modified electrodes can provide a higher areal concentration of accessible surface-bound catalysts compared to a traditional monolayer-based assembly.[37]

A photocatalytic process commonly starts with exciting antenna molecules by photons absorption, then they sensitize other components *via* an energy transfer (EnT) process, and finally, the energy is delivered to catalytic sites for charge separation to generate redox equivalents for chemical transformation. This cascade of processes is reminiscent of the natural light-harvesting complexes (LHC) in photosystem I and II (PS-I/II), where more antenna pigments are assembled than the special pairs; such system can be achieved in supramolecular assemblies like MOFs. Alternatively, the initially generated excited sensitizers can directly involve in charge-separation processes with appropriate complementary units, where the resulting charges (or redox equivalents) can take part in catalysis or initiate a migration chain to be carried away for further utilization.[15, 38] Such systems have essentially the one-to-one ratio of the antenna component to the charge separation unit and are a simplified molecular or

supermolecular version developed for synthetic ease. Nevertheless, a good photocatalyst must have high light absorptivity producing long-lived excited states to transfer the energy into relevant sites for charge separation, and importantly, a slow charge recombination rate is required for the system to initiate charge migration and/or driving chemical transformations. Photoinduced charge transfer (PCT), involving chromophoric linkers and metal SBUs,[39] or post-synthetically incorporated redox species (such as chromophores,[40-43] complexes,[44-46] metallic clusters,[47-49] and semiconducting nanostructures[50]) may prolong the overall lifetime of excited states for their meaningful utilization in catalysis. Therefore, understanding PCT between different photo-responsive moieties within MOFs would give insights for the design of highly efficient MOF-based photocatalysts.

The assembly of photoactive components in MOFs also makes them excellent candidates for luminescent sensing, where the detection of various analytes is based on the "turn-off" or "turn-on" process triggered by the PCT process. The "turn-off" mechanism involves the binding of analytes at the light-responsive component to quench its fluorescence *via* PCT between the excited fluorophore and the analyte. Such a quenching mechanism is not always accurate since other non-analyte factors may 'contaminate' the results by suppressing the fluorescence *via* undesired nonradiative decay. In contrast, the "turn-on" detection can be more accurate as it involves the specific analyte binding at one of the subunits of a donor (D)-acceptor (A) dyad to suppress the intra-molecular PCT and thereby facilitating a fluorescence recovery. This is commonly achieved by altering the electronic and/or energetics of the lowest unoccupied molecular/crystal orbital of the acceptor subunit upon analyte binding (possibly by providing electron density from the analytes), which significantly inhibits the intramolecular ET from donor to acceptor. The complete accessibility of such binding sites that are arranged in the proximity of photo-active components makes the MOF-based sensing system ideal and quick. These components, chosen based on their relative electronic properties, provide opportunities to tune the PCT within MOFs. Thus, understanding the underlying properties will guide future development of MOF-based sensors.

Many contemporary works suggest that MOFs are emerging as optoelectronic compositions. Thus, photoinduced exciton generation and relevant harvesting via EnT, as well as electrode-induced charge transport through redox hopping are important steps; these phenomena have been diligently reviewed in several recent articles.[51-54]. Given that the PCT is another critical step in the same context, here we systematically discuss the excited-state properties of MOFs that drive photocatalysis, photoelectrocatalytis, and emission sensing. As such, screening MOF literature leads to many hits that report some short of photoinduced processes, where many interesting observations have been attributed to PCT in some-what hand-waving fashion. Surprisingly, the proposed correlation of the underlying mechanism to a PCT is found to be made without the key spectroscopic data identifying the PCT intermediates. For that reason, we focus our discussion on the works that elaborate PCT

with state-of-the-art spectroscopic techniques (*e.g.,* optical transient absorption (OTA/TA), electron paramagnetic resonance (EPR) spectroscopy, *etc.*) in MOF systems. We believe the understanding will shine a light on the future development of MOF photocatalysts and sensors.
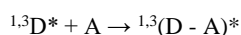
I. Background of PCT

PCT processes may involve a transfer of a high energy electron from a photo-excited D to the LUMO of A, which can be described as follow:[55]
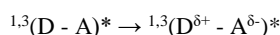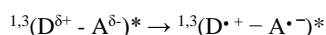
Step 1: Excitation of D

$$D + A \rightarrow {}^{1,3}D^* + A$$
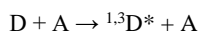
Step 2: Delocalization of excited states in D-A pair

$${}^{1,3}D^* + A \rightarrow {}^{1,3}(D \text{ - } A)^*$$

Step 3: Charge separation

$${}^{1,3}(D \text{ - } A)^* \rightarrow {}^{1,3}(D^{\delta+} \text{ - } A^{\delta-})^*$$

Step 4: Formation of radical ion pair

$${}^{1,3}(D^{\delta+} \text{ - } A^{\delta-})^* \rightarrow {}^{1,3}(D^{\bullet +} - A^{\bullet -})^*$$

Step 5: Forming of electron transferred state

$${}^{1,3}(D^{+\cdot} \text{ - } A^{-\cdot})^* \rightarrow D^{\bullet +} + A^{\bullet -}$$
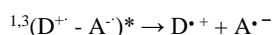
(Singlet and triplet excited states are denoted by (1,3) in the superscript)

Commonly PCT starts with the vertical photoexcitation of the D (Step 1). Electrons are excited from its highest occupied molecular orbitals (HOMO) energy level to higher energy level ($E_{ox}^{D*} = E_{ox}^{D} + E_{0,0}$). This excited-state can get delocalized over the D-A assembly (Step 2). In crystalline MOFs, the densely and precisely packed chromophores offer unique excited-state dynamics that can be fundamentally different from other assemblies like the stacked chromophore aggregates. The excited-states in MOFs can be delocalized over multiple chromophores defining molecular excitons which undergo a fast-displacement *via* an efficient hopping process,[56, 57] and drive electron transfer (ET) with complementary chromophore or redox species with the appropriate alignment of frontier molecular/crystal orbitals.[58-60] However, the key feature that can be availed in MOF is the tunable relative concentration of the complementary redox species. For those frameworks that assemble two types of linkers (*e.g.,* pillar-paddlewheel MOFs) or the ET pairs are constructed from the linkers and metal SBUs, a long-distant EnT is not required. In contrast, for systems where the complementary moieties are sparse specifically post-synthetically installed, an efficient EnT becomes a key step. The occurrence of ET (Step 3) will lead to the formation of a radical ion pair - the driving force of which would depend on the energy gap between the excited-state oxidation potential of the donor (E_{ox}^{D*}) and the ground-state reduction potential of the acceptor (*i.e.* when the ionization potential (I_{D*}) of the excited D* is lower than the sum up of electron affinity of A and the Coulomb

energy of the separated radicals). At each step, however, the excited species can recombine and relax back to the ground state both via radiative (emission of light) and non-radiative processes. Nevertheless, a useful strategy would be to prolong the lifetime of the charge-transferred states, which is commonly achieved by spatially displacing the charged species or changing the structure of the ET-complex by delocalization.[55]

An alternative case can be considered where the acceptor component is excited. In this scenario, the LUMO (or LUCO, lowest unoccupied crystal orbitals of MOFs) of the D still being higher in energy relative to the excited-state oxidation potential of the acceptor (E_{ox}^{A*}), the hole-polaron in the excited acceptor is transferred to the donor at the ground state. This alternate process can be described from a perspective that depicts an electron being transferred from the donor (in the ground state) to the excited acceptor, this process involves HOMO or HOCO (highest occupied crystal orbitals) of the relevant components. Thus, both processes are described through a generalized charge transfer (CT)-probability, which will involve the lowest unoccupied or highest occupied orbitals and be governed by their energetics and respective coupling terms.

Marcus theory has been widely used to analyze various CT reactions between inorganic redox couples in homogeneous systems,[61] electrochemical reactions on solid electrodes,[62, 63] as well as in biological[61] redox enzymes such as cytochromes,[64] peroxidase,[65, 66] and photosynthetic enzymes.[67, 68] The PCT processes among the redox entities in MOFs can also be analyzed within the frameworks of Marcus theory,[61, 69-72] where the CT rate constant (k_{CT}) is expressed as the function of the free energy ΔG^0:

$$k_{CT} = \frac{2\pi}{\hbar} H_{DA}^2 \frac{1}{\sqrt{4\pi\lambda_t k_b T}} \exp\left[-\frac{(\lambda_t + \Delta G^0)^2}{4\pi\lambda_t k_b T}\right] \tag{1}$$

where H$_{DA}$ represents the electronic coupling between the reactant and product, ΔG^0 is the thermodynamic driving force, and λ_t is the total reorganization energy. The λ_t term is the sum of internal reorganization energy (λ_i) and solvent oscillators (λ_s). The λ_i stems from the oscillators within the redox species and can be determined by the vibrational energy of all molecules in reactants (R) and products (P), whereas the λ_s is calculated via the dielectric continuum model of the solvent. While the major factor defining the k_{CT} for a reaction is either the H$_{DA}$ or ΔG^* at a given temperature and has been well established over the last several decades, MOF can manifest unique opportunities to be exploited relative to those in molecular or hybrid homogeneous systems. This is because the fixed and structure-dependent positioning of the D-A species defining the $H_{DA} \propto e^{-\beta(r-r_0)}$, where r$_0$ is the contact distance between D and A, and β is the distance and dielectric dependent decay factor of the tunneling electron wave-functions. The microporous MOFs offers various features such as the structural rigidity, the unique solvent orientation (relative to the bulk), and the micro/local environment -these can play critical role defining the λ$_t$ that may be difficult to achieve in a homogeneous macromolecular system and can only be observed in elegant biological design.

Figure 1a depicts the potential energy diagram of reactants and products as a function of nuclear coordinate in an
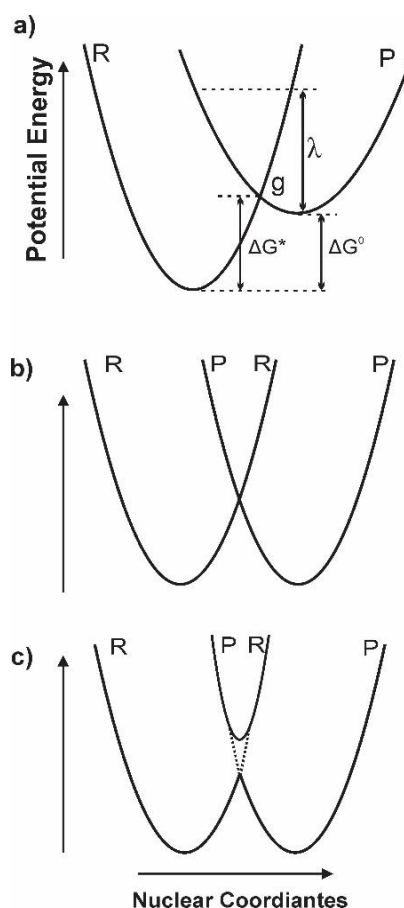
Figure 1. a) Potential energy diagrams of reactant (R) and product (P) for endergonic reaction. Potential energy surface for the R and P in b) nonadiabatic ET with insignificant and c) adiabatic with strong electronic coupling (H$_{DA}$).

endergonic reaction. A CT process can occur at the intersection of the potential energy surface where the overlap of wavefunctions of R and P reaches maximum. The activation energy ΔG^* required to pass this intersection is mathematically related to ΔG^0:

$$\Delta G^* = (\lambda_t + \Delta G^0)^2/4\lambda_t \tag{2}$$

Equation 2 explains a quadratic relation of the rate with the driving force – with the highest rate observed when the driving force is the same as the reorganization energy. Since a CT is too fast to allow nuclei of R and P to shift their position,[61] the electronic coupling element H_{DA} is distance-dependent and a strong coupling will enhance the CT probability in the adiabatic fashion (**Figure 1c**). The ΔG^0 can be calculated by the Rehm-Weller equation (3);[73, 74] these values often used to guide the design for the feasibility of PCT between the D and A species.

$$\Delta G_{CT}^0 = e\left(E_{ox}^D - E_{red}^A\right) - \Delta E_{0,0} - \Delta G^0(\epsilon) \tag{3}$$

Here E_{ox}^D and E_{red}^A represent the ground state oxidation and reduction potential of D and A respectively; $E_{0,0}$ is the first excited-state energy of D. The $\Delta G^0(\epsilon)$ is the dielectric correction term based on the Born equation (4):[74]

$$\Delta G^0(\epsilon) = \frac{e^2}{4\pi\epsilon_0\epsilon_S R_{DA}} + \frac{e^2}{8\pi\epsilon_0}\left(\frac{1}{r_D} - \frac{1}{r_A}\right)\left(\frac{1}{\epsilon_{ref}} - \frac{1}{\epsilon_S}\right) \qquad (4)$$

where ϵ_0 is the permittivity of free space, ϵ_s is the static dielectric constant of the solvent, ϵ_{ref} is the dielectric constant of solvent where the redox potentials were measured. The first term of the eq-4 reflects the interaction energy between the D A radical ions with radius r_D and r_A at a center to center distance R_{DA}, where the second term corrects the difference of ion solvation between a solvent of interest and solvent where redox potential was measured.

II.PCT in MOFs

PCT in MOFs begins with the photonic energy absorption by either chromophoric linkers, metal SBUs, or both. Here, the CT can occur within intrinsic structural components of the framework (*e.g.* a linker, metallic building blocks); alternatively, a guest component that was installed or infiltrated into the framework can be involved. PCT in MOFs can involve either a linker-to-metal (LMCT), linker-to-linker (LLCT), or host-guest components as long as it satisfies the requirements: (*i*) the relative energetics of the frontier orbitals of D-A pair are properly aligned to drive a CT in an energetically favorable manner; and (*ii*) the center-to-center distance of the D-A dyad lies within the range of the exciton delocalization radius of D. We will discuss the PCT in MOF within the intrinsic components and installed/infiltrated system.

II.A. PCT between intrinsic structural components as donor-acceptor pair

PCT between intrinsic structural component would either require MOFs with one type of linker and redox-active metal node with appropriate coordination geometry defining its potential energy and ligand-field transitions or two redox-active linkers (with inactive metal ions (e.g. Zn^{II}, Zr^{IV}, etc) based node) as seen in pillar-paddlewheel type structures. Recently, the intrinsic LMCT between linkers and metal building blocks within the framework has been extensively studied using spectroscopy. The Huang group has explored the excited states and CT dynamics within a cobalt Zeolitic Imidazolate Framework is known as ZIF-67 (**Figure 2a.**) using various steady-state and transient spectroscopic techniques such as ultraviolet-visible (UV-Vis), femto- nanosecond (optical) transient absorption (fs/ns-OTA), and X-ray transient absorption (XTA) spectroscopy.[39] **Figure 2c** shows the UV-Vis-near IR absorption spectrum of ZIF-67 film. The characteristic absorptions at 300, 590, and 900-1400 nm (broad) are attributed to an LMCT, a higher-energy $[^4A_2(F) \rightarrow {}^4T_1(P)]$, and a lower-energy $[^4A_2(F) \rightarrow {}^4T_1(F)]$ ligand field transitions as depicted in **Figure 2b.** The fs-OTA spectra recorded by exciting the MOF sample at 1000 nm (*i.e.* $[^4A_2(F) \rightarrow {}^4T_1(F)]$ transition) highlight several key processes when probed in the visible region (475-700 nm). These include a ground state bleach (GSB) due to a depletion of $^4A_2(F)$ population (**Figure 2d**; at 520-600 nm), and a weak broad transient absorption at 640-700 nm for the excitation of the populated $^4T_1(F)$ state (**Figure 2d.** inset). The excited $^4T_1(F)$ state
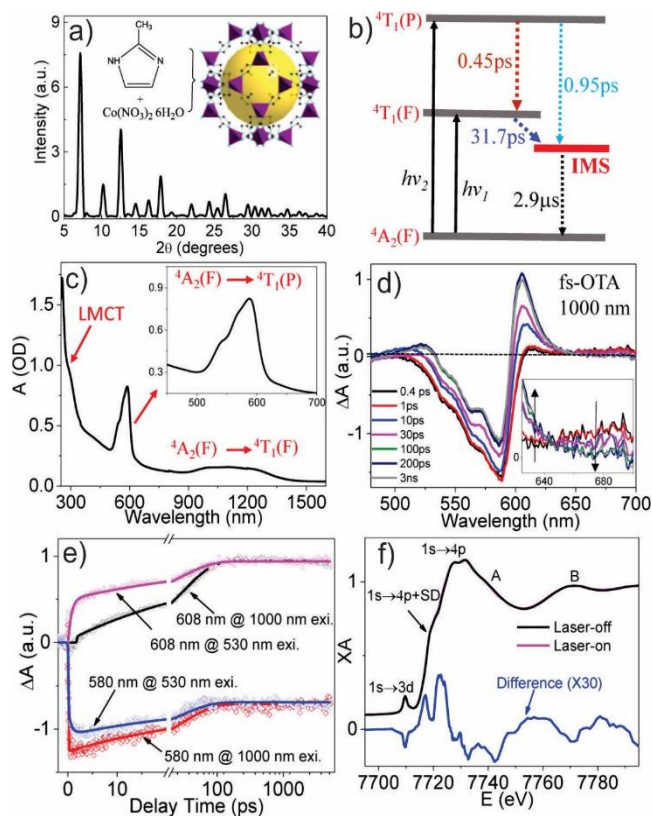

Figure 2. a) Chemical structure and powder XRD patterns of ZIF-67; b) The schematic representation of energy diagram of Co^{2+} (T_d) and excited state relaxation processes in ZIF-67; c) UV-Vis-Near IR absorption spectrum of ZIF-67; d) fs-OTA spectra of ZIF-67 at 1000 nm; e) Kinetics at 608 nm and 580 nm in fs-OTA spectra of ZIF-67 after 1000 nm and 530 nm excitation. f) XANES spectrum of ZIF-67 at Co K-edge before (laser-off) and 500 ps after laser excitation (laser on). Reproduced with permission from ref. 39. Copyright 2016, American Chemical Society.

decays to form a long-lived intermediate state (IMS) which can be seen by the rise of absorption band centered at 525 nm and 605 nm. The excited-state dynamics were globally analyzed with the bi-exponential fitting of the fs-OTA (**Figure 2e**) as well as the ns-OTA kinetic data, probed at 580 and 608 nm, respectively. From these fittings, the authors determined a fast 31.7 ps component attributed to the IMS state formation and two longer, 0.64 and 9.2 µs, components as the lifetime of IMS (weighted average lifetime of 2.9 us). The authors probed the dynamics of the higher $^4T_1(P)$ state by selectively exciting the sample with a 530 nm pump (compared to a 1000 nm light that preferably excites the $^4T_1(F)$ from $^4A_2(F)$ ground states). A similar global analysis of the kinetic data reveals two additional time-constants: a 0.45 ps lifetime attributed to the $^4T_1(P) \rightarrow {}^4T_1(F)$ relaxation, and a new 0.95 ps component assigned to the direct IMS formation (*i.e.*, $^4T_1(P) \rightarrow$ IMS). A similarity between the OTA spectra of the IMS state and the second derivative of the GSB led the authors to postulate that the observed IMS state is a long-lived charge-separated (CS) state. To prove the hypothesis, the authors recorded XANES spectra (**Figure 2f**) before (*i.e.* under 'laser-off' condition) and after 527 nm excitation (*i.e.* a 'laser-on' -excited condition), which exhibited a broad positive transient absorption between 7714.9-7725.3 eV where 1s-4p

shake-down[75] and 1s-4p transition[76] occur. This characteristic signature indicates a red-shifted transition, *i.e.* the edge of cobalt-center shifts to lower energy, possibly due to the photoreduction of Co^{II} *via* LMCT. This long-lived charge-separated state shows the potential of ZIF-67 in photocatalysis in energy conversion processes.

In another robust MIL-100(Fe) MOF, Hanna and coworkers reported a long-lived excited state with an LMCT character resulting from CT from an excited 1,3,5-benzenetricarboxylate linker to the Fe$_3$-μ_3-oxo clusters/SBU.[77] Their fs-OTA spectra (**Figure 3b**) and related dynamical data suggest that such LMCT state in MIL-100(Fe) persists over hundreds of nanoseconds. Further characterization of the LMCT process involved X-ray transient absorption (XTA) spectroscopy. The XTA collected at multiple delay times (**Figure 3c**) indicates an increased electron
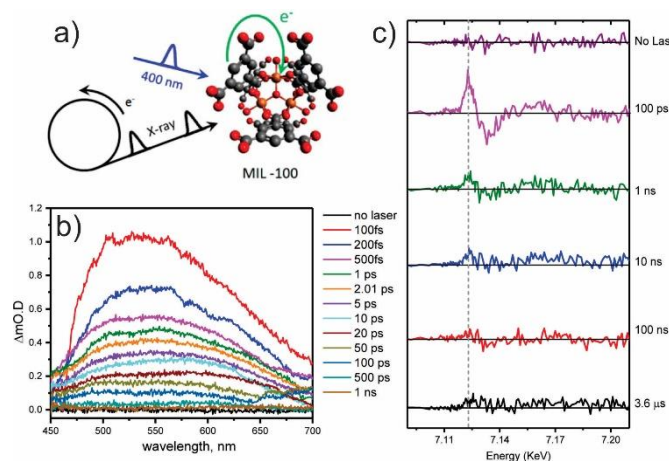

Figure 3. a) Schematic illustration of LMET from the excited linker to Fe$_3$-μ_3-oxo clusters; b) OTA spectra collected at different time delays (λ_{ex}=400 nm); c) XTA difference spectra obtained at multiple time delays for MIL100(Fe) Reproduced with permission from ref. 77. Copyright 2017, American Chemical Society.

density at the iron sites (signal edge at 7.12 KeV) as expected for an LMCT process, which corroborates well with the finding from the fs-OTA spectra. The XTA signal observed up to 3.6 μs delay time confirms the long-lived CT excited state, which could be stabilized by electron delocalization within the Fe$_3$-μ_3-oxo clusters, which can be a good strategy to achieve a useful long-lived PCT state.

Titanium dioxide has been explored as promising photocatalysts due to the low-lying Ti^{IV}-Ti^{III} valence exchange band featuring UV responsive bandgap. This unique electronic property has made this material a good photoanode layer in dye-sensitized solar cells. This has triggered an extensive investigation on the band structure of titanium oxide-based MOFs for the possible PCT involving organic linkers.[78-80] In one such study, Portillo *et al.* prepared amino-UiO-66 derivatives denoted as NH$_2$–UiO-66(Zr/Ti). These hybrid porous compositions were constructed from deprotonated 2-aminoterephthalic acid (ATA), with exchanged Ti species up to 35% onto the Zr-oxo nodes, and were investigated for the role of Ti-doped Zr-oxo clusters in PCT.[81] The diffuse reflectance TA spectra (**Figure 4b**) of NH$_2$–UiO-66(Zr/Ti-35%) displayed two absorption bands at 450 and 540 nm recorded at 3 and 184 μs

delay time after the 355 nm laser pulse (samples with lower Ti doping have similar, analogous spectra). The fitting of kinetic profiles (**Figure 4c**) monitored at 450 nm featured two lifetimes τ_1 = 8.6 ± 2.3 μs (45%) and τ_2 >200 μs (55%); whereas the 540 nm profile has a rising (single) component with τ_{rising} = 8.5 ± 2.5 μs. The 450 nm TA band was assigned as the excited-state transition in the triplet manifold of NH$_2$–UiO-66(Zr/Ti), which displays a faster decay profile mediated by molecular oxygen. With the similarity between the time constant for the fast decay component measured at 450 nm absorption (*i.e.* τ_1 = 8.6 ± 2.3 μs) and the rising lifetime of 540 nm band (τ_{rising} = 8.5 ± 2.5 μs), the authors inferred that the formation of the transient species
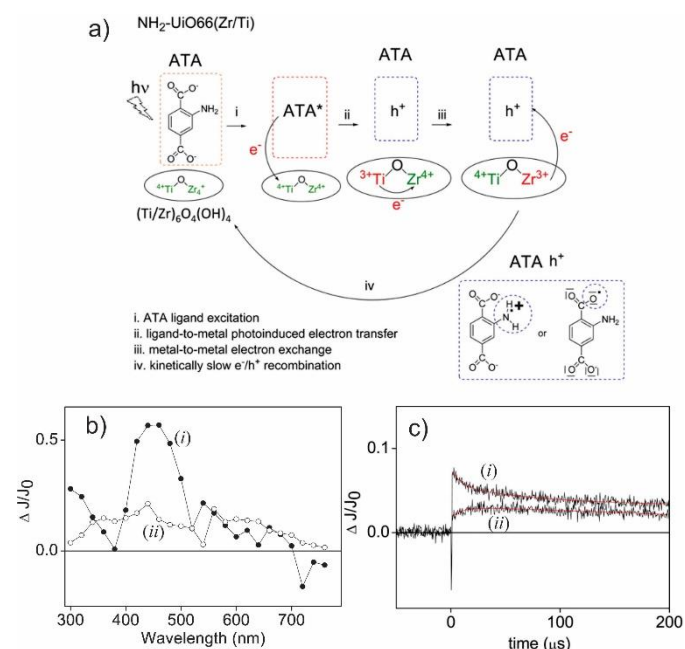
Figure 4. a) Scheme depicting the Ti^{3+}−O−Zr^{4+} species as mediator for LMET in NH$_2$−UiO-66(Zr/Ti); b) UV−vis diffuse reflectance TA spectra recorded (*i*) 3 and (*ii*) 184 μs after 355 nm laser pulse under nitrogen atmosphere for NH$_2$−UiO-66(Zr/Ti-35%). c) Kinetic profile monitored at (*i*) 450 and (*ii*) 540 nm after 355 nm laser pulse under nitrogen atmosphere for NH$_2$−UiO-66(Zr/Ti-35%). Reproduced with permission from ref. 81. Copyright 2017, American Chemical Society.

associated with the 540 nm absorption commences (~ 40%) from the decay of the triplet state. The 540 nm absorption is assigned to the conversion of Ti^{4+} to Ti^{3+}, verified by an analogous homogeneous quenching experiment between ATA and Ti^{4+}. Based on these TA results, it was proposed that LMCT can occur from an ATA* to the (Ti/Zr)$_6$O$_4$(OH)$_4$ node forming Ti^{3+}−O−Zr^{4+} species that can live long enough to possibly drive chemical transformation. This result can be compared to an analogous experiment by Gascon and co-workers who reported that the pristine NH$_2$-UiO-66(Zr) MOF (*i.e.* without any Ti-dopant) does not facilitate any LMCT process. This is due to a larger band gap for the Zr-oxo cluster, which is aligned in a way that does not facilitate electronic interaction with the organic linker. Therefore, the photoexcitation leads to a linker-centered, short-lived excited-state within the pristine NH$_2$-UiO-66(Zr) MOF.[82]

On the other hand, the electronic and redox properties of the linker can also be a key factor to modulate the LMCT to Ti-oxo clusters. Padial *et al.* reported a hydroxamate-based MOF MUV-11 constructed by reacting benzene-1,4-dihydroxamic acid (H$_4$bdha) with titanium (IV) isopropoxide in dimethylformamide (DMF). The chelating moiety in this linker is different from the typical carboxylates. Computational modeling revealed that a hydroxamate siderophore binder results in a drastic change of the frontier orbitals in MOF and thereby suppress the CT kinetics (*i.e.* less likely to undergo LMCT from the hydroxamate linker to Ti clusters).[83] In common titanium-carboxylate based MOFs, such as Ti-terephthalate (*i.e.* MIL-125-NH$_2$ with a chemical formula Ti$_8$O$_8$(OH)$_4$(bdc-NH$_2$)$_6$, where bdc is 1,4-benzenedicarboxylate), it has been established that photoexcitation will lead to LMCT generating photo-reduced Ti^{III} which can be probed by EPR spectra.[84] The electronic density of states (DOS; **Figure 5a**) display that for the carboxylate MOFs, HOCO is localized at the organic linker, whereas the LUCO is titanium-node centered. Such frontier orbital alignments provide a thermodynamically favorable
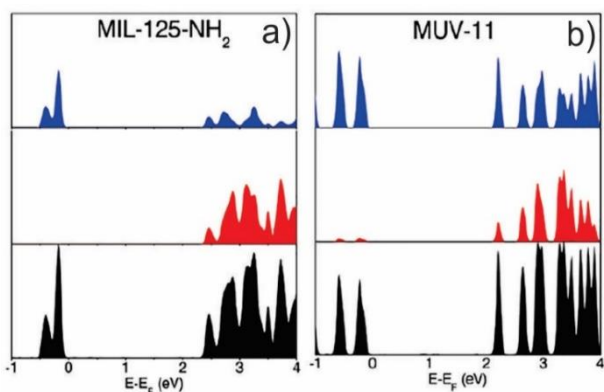
Figure 5. Total (black) and projected (Ti in red and ligand in blue) density of states for a) MIL-125-NH$_2$, b) MUV-11. Reproduced with permission from ref. 83. Copyright 2019, American Chemical Society.

driving force with a negative LMCT energy. In contrast, the Ti-hydroxamate MOF -*i.e.* the MUV-11 exhibits a linker-centered LUCO (**Figure 5b**) with a high orbital contribution of *ca.* 70%. The electronic structure indicates linker localized excited-state in MUV-11 with more or less no driving force for LMCT, which is consistent with the fact that photoexcitation did not produce any paramagnetic signal from photoreduced Ti^{III} species (as opposed to the common Ti-carboxylate systems). As a result, the MUV-11 did not display any photocatalytic HER activity. This study demonstrated that the electronic properties of metal SBUs and organic linkers (as function of the electronic properties of their side group functionality and the binding moiety) can significantly impact the PCT within the frameworks, which should be planned in the design for MOF-based catalytic systems.

Fullerenes and their derivatives are widely used as excellent electron acceptors in PCT processes[85], especially in organic photovoltaics, where they aggregate and form electron transport media. Likewise, installing fullerene within the MOF pores can serve both purposes: as a PCT component and an electron-transport channel, depending on the loading density.
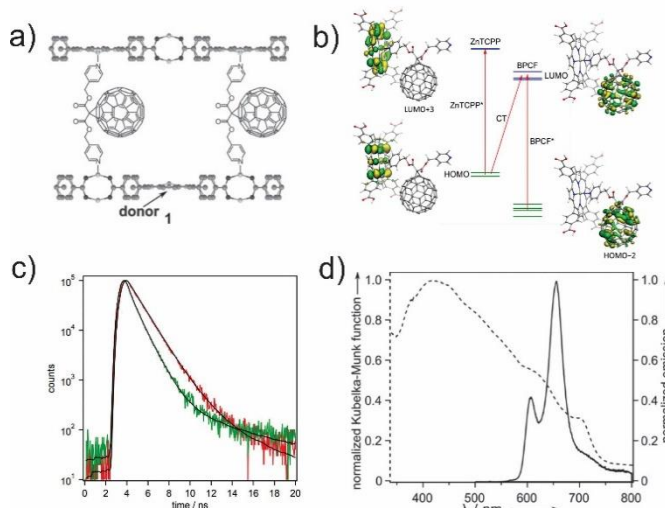
Figure 6. a) Structure of porphyrin- fullerene pillar-paddlewheel MOF where BPCF serving as based both energy and electron-accepting linkers in the crystalline framework; b) Computationally obtained energy diagram and molecular orbitals of the C$_{60}$–ZnTCPP molecular dyad. Red arrows show three types of excitations anticipated in this system; c) Transient fluorescence decays of C$_{60}$@PMOF (green) and Zn$_2$(ZnTCPP) (red); d) Normalized diffuse reflectance of BPCF (dashed line) and emission of the two-dimensional porphyrin-based framework Zn$_2$-(ZnTCPP) (solid line). Reproduced with permission from ref. 86. Copyright 2016, Wiley-VCH.

In one such assembly, the photophysical behavior of fullerene-based MOF was investigated. The Shustova group prepared a multilayered pillar-paddlewheel crystalline framework containing porphyrin-fullerene dyad as D-A pair.[86] The MOF can be defined as slipped-layers of tetrakis(4-carboxyphenyl)porphyrinato zinc(II) (TCPPZn) formed through zinc-carboxylate based paddle-wheel node, where the fullerene derivative, bis(pyridin-4-ylmethyl)-3'H-cyclopropa-[1,2](C$_{60}$-Ih)[5,6]fullerene-3',3'-dicarboxylate (BPCF), served as the pillar-binding two Zn centers, one of TCPPZn and the other from the node at the neighboring layer (**Figure 6a**). The absorption of BPCF (A) and emission of ZnTCPP indicate a significant spectral overlap as the requirement of Förster resonance energy transfer (FRET) from D to A (**Figure 6d**). Based on the fluorescence lifetime quenching (**Figure 6c**) of ZnTCPP (*i.e.* from 1.07 to 0.54 ns), the energy-transfer efficiency and rate constant were estimated to be 49.5% and 9.18×10^8 s^{-1}, respectively. The Förster critical radius (R$_o$) was estimated as 18.8 Å by calculating the spectral overlap function J (= 2.34×10^{-15} cm^3 M^{-1}), which is longer than D-A distance extracted from structural data. Besides FRET, the authors noted that PCT can also be responsible for the lifetime quenching of ZnTCPP. However, this presumption was only supported by time-dependent DFT calculations that showed that the charge-transfer excitation has a similar energy to that of C$_{60}$-based excitations (**Figure 6b**) and no direct characteristic spectral evidence was presented. Thus, thermodynamics of FRET and CT processes are predicted to be comparable.

II.B. PCT between non-framework complementary D-A pair

Given that crystalline MOFs can be used as a solid architectural platform, the available pore can be systematically utilized to host exogenous species other than the solvent. These complementary chromophores and/or redox-active species, in molecular form, can be installed at a precise location by, for example, postsynthetic modifications of side-chain functionality of linker or at the node (other postsynthetic methods such as exchange and ligand incorporation can be also used, *vide infra*). Alternatively, a diffusive infiltration can be used to fill (pack) the pore with the complementary species.

II.B.1. Systems with postsynthetically installed/anchored component

Zirconium MOFs have become popular due to their robust nature and electronic properties that are relevant for photophysical studies including PCT. Being a group-IV transition metal, Zr_6^{IV}-oxo node can be anticipated similar optoelectronic behavior like that of a Ti^{IV}-oxo derived node that frequently features an LMCT from excited organic linkers.[38] However, computational studies suggest that the conduction band of zirconium-oxo node lies 2 eV wider than that of the benzenedicarboxylate linker due to high energy zirconium 4d orbitals.[87] Thus, a photo-induced LMCT from a common π-conjugated linker to Zr_6^{IV}-oxo node is unlikely to occur unless the excited state oxidation potential of the linker is unusually high in energy. This electronic property of the Zr_6^{IV}-oxo nodes makes them unique in a way that the linker orbitals do not electronically interact with. As a result, the Zr_6^{IV}-oxo nodes become optoelectronically "inert" in the UV–vis region relative to most π-conjugated organic linkers. Hence, Zr_6^{IV}-oxo derived frameworks provide desired chemically and mechanically robust platforms where various photophysical studies including PCT can be examined among different linkers and other components as a function of their crystallographic position. The Zr^{IV}-ions may exert a 'heavy atom' effect facilitating singlet-to-triplet intersystem crossing processes, but no study has established this yet. Nevertheless, the chemical constituents of such metal-oxo node may play a key role in defining the CT kinetics.

Most Zr_6^{IV}-oxo MOFs can host a wide range of secondary organic or inorganic species, which further extend the possibilities of realizing donor-acceptor dyad systems. This is because, a majority of the Zr_6^{IV}-oxo MOFs possess large pore ranging from 10Å to over 50Å depending on the topological net.[88-93] These pores are suitable to incorporate complementary species including small organic,[34, 94] organometallic[95-99], cluster,[49, 100-103] or even small enzyme.[104-106] Furthermore, common Zr_6^{IV}-oxo SBUs construct 12 or 8–carboxy connected MOFs: thus, an unsaturated 8-connected Zr_6-oxo node can be exploited to install carboxy-terminated redox species *via* a well-established process called solvent assisted linker incorporation (SALI).[34, 95, 107] Alternatively, a 12 connected MOF (*e.g.* UiO-66) with the variable extent of defects (i.e. missing linkers, capped with a monocarboxylate such as formate) can be defect-exchanged/engineered.[108-110] Both these postsynthesis processes are technically the same as they involve the
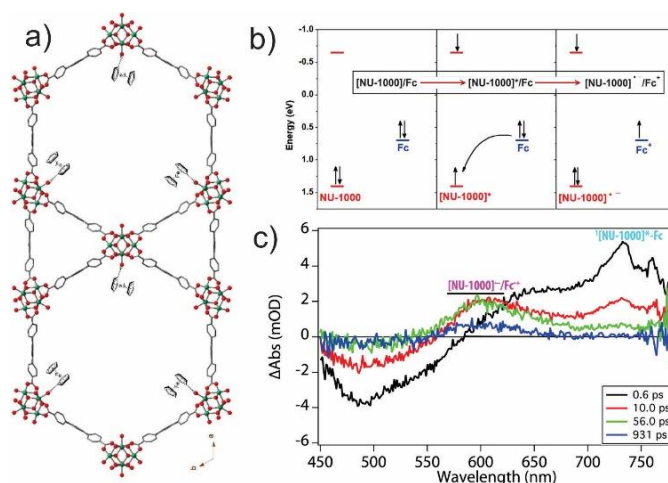
Figure 7. a) Structure of Fc@NU-1000; b) energy diagram depicting the PET process from Fc to excited NU-1000 in Fc@NU-1000; c) Representative fs-TA spectra of Fc@NU-1000 under the excitation of 400nm. Reproduced with permission from ref. 95. Copyright 2018, American Chemical Society.
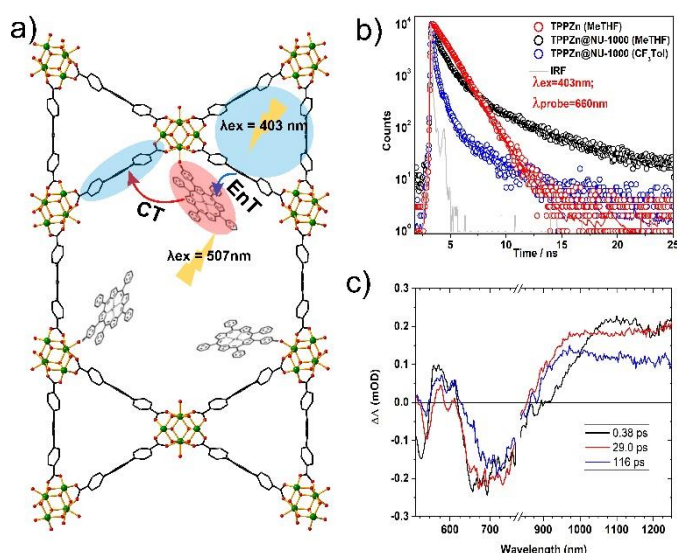
replacement of non-framework ligands (like hydroxy and carboxy) with an incoming carboxylate or phosphonate.[111]

In this context, a well-known Zr_6^{IV}-oxo MOF NU-1000 has been used as a host platform. Here, an assembly of deprotonated 1,3,6,8-tetrakis(p-benzoicacid)pyrene linker (TBAPy) acts as an antenna for photon harvest. A study reported by the Deria group showed that immobilizing carboxy-ferrocene (Fc) at the Zr-oxo node forming Fc@NU-1000 (**Figure 7a**) quenches the MOF emission *via* a CT from the Fc to the photo-excited TBAPy (**Figure 7b**).[95] It is important to note that less than one Fc per four TBAPy linkers is enough to reach the saturation quenching, this observation indicates to another interesting feature in MOF: an efficient EnT enhances the quenching perimeter of a redox quencher. The fs-TA spectroscopic data of Fc@NU-1000 highlights the instant appearance of an intense singlet ($S_1 \rightarrow S_n$) excited state absorption (ESA) at 730 nm (**Figure 7c**; TA spectrum at 0.6 ps); this signature, is reminiscent to that of excited pristine NU-1000, was assigned as the [NU-1000]*/Fc. The singlet excited population then quickly decays to a new ESA appearing at 600 nm and assigned as [NU-1000]•⁻/Fc⁺. Given a close Fc-pyrene distance (*ca.* 10 Å), the k_{CT} was determined (from the rise time of 600 nm band) to be very efficient 7.4×10^{10} s⁻¹ (τ_{CT} = 9 ps) with a relatively slow thermal charge recombination (τ_{CR} = 430 ps). Interestingly, solvent-dependent k_{CT} data determined from the emission quenching experiments (using time-resolved fluorescence data) revealed that the CT process is nonresponsive to dielectric modulation. This is because the node-bound Fc-moieties experience a polar microenvironment formed by the protruding hydroxyl/aqua ligands at the Zr_6^{IV}-oxo node. Thus, the CT process in Fc@NU-1000 involves a high 'solvent' reorganization energy (λ_o) to drive [NU-1000]•⁻/Fc⁺ formation. Partial capping of the hydroxyl/aqua ligands was seen to slightly increases the rate.[38]

In an attempt to emulate the functionality of the chlorophyll based LHCs, Deria and coworkers showed that complementary pigment-assemblies within MOFs can be a viable way. For that, they first post-synthetically anchored a

tetraphenylporphyrinato zinc(II) (TPPZn) derived complementary pigment within the 1D pores of NU-1000 MOF forming a D-A system.[107] This design is based on the appropriate alignment of the ground and excited-state redox potentials of donor and acceptor in a way that it facilitates an EnT from the excited MOF (*i.e.*, NU-1000*) to the TPPZn forming TPPZn*. Here, the excited TBAPy linker assembly in the framework serves as the antenna to harvest photonic energy and efficiently deliver it to the adjacent TPPZn anchored on the Zr-oxo node via FRET ($k_{EnT} \approx 4.7 \times 10^{11}$ s^{-1}; τ_{EnT} = 2 ps; **Figure 8a**).[107] Given that the excited-state oxidation potential of [TPPZn]* lies 0.54 eV higher than the ground-state reduction potential of NU-1000, a spontaneous CT was observed from [TPPZn]* to NU-1000. The process can be considered as the excited TPPZn pigment forming a special pair like the system with a neighboring TBAPy linker to drive the CT. The PCT was studied *via* transient emission that revealed a solvent polarity dependent rate: a k_{CT} = 6.2×10^8 s^{-1} and 1.2×10^{10} s^{-1} (*i.e.* τ_{CT} ~ 1.6 ns and 80 ps) in 2-methyltetrahydrofuran (MeTHF) and trifluorotoluene (CF$_3$Tol) solvents, respectively. This is an interesting finding for two reasons. First, the highest rate recorded for the TPPZn@NU-1000 is about one order magnitude slower than that was observed for the Fc@NU-1000 system ($k_{CT} \approx 1 \times 10^{11}$ s^{-1}; τ_{CT} ~ 10


Figure 8. a) Scheme of photoinduced electron/energy transfer in a typical TPPZn@NU-1000 structure, depicting the energy and charge transfer between TPPZn and Pyrene under the excitation of 403 and 507nm. b) Transient emission decay profiles of NU-1000, TPPZn, and TPPZn@NU-1000 in two solvents (λ_{ex} =403 nm, λ_{probe} = 660 nm); c) Representative fs-TA spectra of Fc@NU-1000 under the excitation of 400nm. Reproduced with permission from ref. 107. Copyright 2019, American Chemical Society.

ps) even though the Zn-pyrene distance (*ca.* 8.7 Å) is slightly shorter than the Fc-pyrene distance. This is possible due to a negligible internal reorganization energy for the Fc-centered redox process in a way that the driving force (ΔG^0) matches with the total reorganization energy. Second, the TPPZn@NU-1000 composition displayed significant solvent polarity dependent rate: *ca* 20-fold difference in k_{CT} going from MeTHF to CF$_3$Tol solvent compared to a negligible solvent response in Fc@NU-

1000. This is because the TPPZn is fixed far from the polar Zr-oxo SBUs compared to the Fc-moiety: d$_{Fe-Zr}$ = 5.6 Å in Fc@NU-1000), where d$_{Zn-Zr}$ = 12.75 Å in TPPZn@NU-1000. The fs-TA spectroscopic data collected for TPPZn@NU-1000 (in CF$_3$Tol solvent) clearly displayed unambiguous signal for GSB (540 nm) and S$_1 \rightarrow$ S$_0$ stimulated emission (660 nm) of TPPZn*; where a broad NIR transient at 976 nm evinced for TPPZn$^{\bullet+}$, and the signal for [NU-1000]$^{\bullet-}$ at ~ 600 nm is obscured by the TA signal of the TPPZn* and its stimulated emission bands. However, the evolution of red-shifted stimulated emission peak of TPPZn* (660 nm → 700 nm) attests to the underlying rise of the [NU-1000]$^{\bullet-}$ (at ~600 nm; blue side of the stimulated emission band) over time. The global fitting of the transient dynamical data probed at 541, 693, and 976 nm revealed a 283 ps charge recombination time constant. The design of this system also highlights an impressive spectral coverage of the system: the TPPZn moiety absorbs light energy complementary to the TBAPy assembly and can be excited directly through its low energy Q band derived transition (at 530 nm) and thus, the TPPZn@NU-1000 composition covers a large (350-650 nm) effective window of the solar spectrum and all of it can lead to the TPPZn$^{\bullet+}$/[NU-1000]$^{\bullet-}$ CT-state formation. Given that the PCT generated charge-carriers in TPPZn@NU-1000 (with a $\tau_{CR} \simeq$ 280 ps) can migrate *via* redox hopping[112-114] through both TBAPy and the TPPZn units, respectively, they can be harvested in photoelectrochemical setup (IPCE $\simeq$ 0.36% at 532 nm, -0.5V *vs* Ag/AgCl).

II.B.2. Systems with postsynthetically infiltrated components

Depending on the size and shape of the pores, a postsynthetic infiltration process may differ. For example, in cage-like pores, one would have to introduce the secondary guest component during synthesis or employ a dynamic window opening facilitated by a linker exchange process. In this 'ship-in-a-bottle' scenario, the incorporated species is larger than the largest pore window and thus, remains 'corked' inside with some limited conformational and rotational flexibility. For 1D pores, however, the complementary species can be diffused inside the pores with varying density. Here, the incorporated species can form a close-packed column or may establish a non-covalent interaction with the aromatic linker, albeit depending on the solvent. While the later system may not provide precise control of the position of the incorporated species, it is a simple method for the preparation of the bulk composition.

PCT processes resulting from triplet excited states have also been studied within host-guest systems in MOFs -the advantage here is a prolonged sensitizer lifetime enabling energy migration and/or driving relatively slower CT with a larger structural reorganization. Larsen and coworkers encapsulated the [Ru(2,2'-bipyridine)$_3$]$^{2+}$ photosensitizer, commonly known as Rubpy, into a MOF in a ship-in-a-bottle fashion. Here, the CoRWLC-2 framework was constructed by a solvothermal reaction of 1,3,5-tris(4-carboxyphenyl)benzene (H$_3$BTB) and Co(NO$_3$)$_2$·(**Figure 9a**).[115] The encapsulated Rubpy exhibits a shorter lifetime of 9.5 ns relative to 600 ns time constant for the pristine Rubpy and this quenching was attributed to PCT
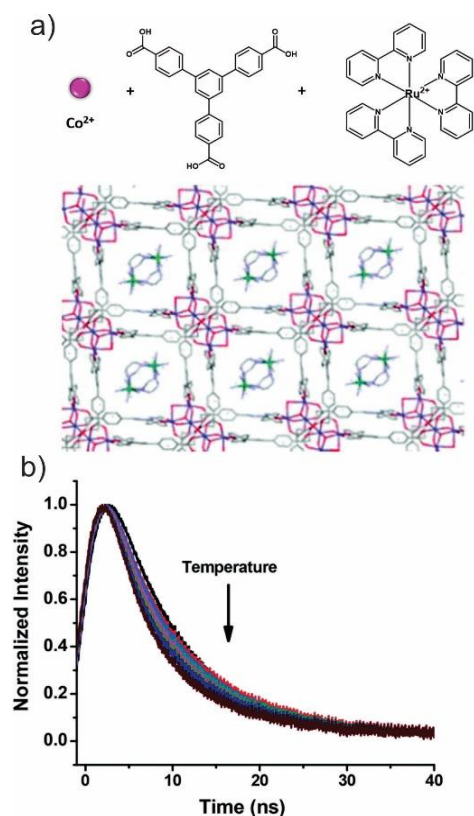
Figure 9. a) Scheme of the formation of CoRWLC-2; b) Temperature dependent emission of CoRWLC-2. Reproduced with permission from ref. 115. Copyright 2018, Royal Society of Chemistry.

between the ^{3}MLCT of Rubby to the Co ion cluster of the node with a $k_{CT} \simeq 10^8$ s^{-1} (**Figure 9b**). This relatively slow rate constant is due to the high reorganization energy (1.6 eV) and a relatively small (0.006 eV) electronic coupling factor (H$_{AB}$) as determined from a temperature depended lifetime data (**Figure 9b**) analyzed in Arrhenius fashion.

This group has extended the ship-in-a-bottle fashion strategy in another system where they co-encapsulated two porphyrin derivatives tetrakis-(tetra 4-sulphonatophenyl)porphyrinato zinc(II) (Zn4SP) and tetrakis-(tetra 4-sulphonatophenyl)porphyrinato iron(III) (Fe4SP) into the cages of HKUST-1(Zn) MOF, denoted as Zn4SP-Fe4SP@HKUST-1 (**Figure 10a**).[116] The authors reported PCT from the triplet excited state, ^{3}Zn4SP to Fe4SP (k_{CT} = 1.1 × 10^4 s^{-1}). This was supported by the ^{3}Zn4SP lifetime quenching by the co-encapsulated Fe4SP (**Figure 10b**). However, no direct spectroscopic evidence was provided to illustrate the mechanistic evolvement of the triplet states in this complicated photophysical cascade process. The PCT process was analyzed with semi-classical Marcus Theory (equation 5) by plotting the rate constant as a function of different sets of parameters:

$$k_{ET} = k_0 \, e^{-\beta(d-R_0)} e^{-(\Delta G^0 + \lambda)^2/4\lambda_t RT} \qquad (5)$$

where k_o is the rate constant associated with barrierless CT, typically on the order of molecular vibration ($\sim$10^{-13} s^{-1}), will happen if it occurs at R_o (i.e. the van der Waals contact distance between D and
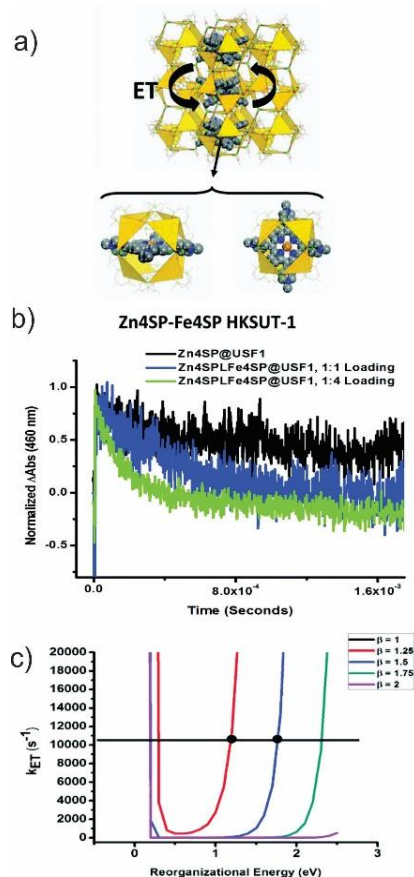
Figure 10. a) Scheme illustrating the relative alignment of Zn4SP and HKSUT-1 in Zn4SP@HKUST-1; b) triplet–triplet absorption decay of Zn4SP@HKUST-1 with varying amounts co-encapsulated Fe4SP suspended in ethanol; c) Plots of calculated k_{ET} versus λ for differing β values using d = 29 Å, k$_0$ = 1 × 10^{13} s^{-1}, R$_0$ = 9.7 Å (for Fe4SP/Zn4SP), ΔG° = −0.61 eV (−14 kcal mol^{-1}) and T = 300 K. The line designates the observed k$_{ET}$ of 11000 s^{-1}. Reproduced with permission from ref. 116. Copyright 2015, Royal Society of Chemistry.

A); here, β is an empirically determined distance-dependent decay constant for the electronic coupling factor, d is the D-A distance, λ_t is the total reorganization energy, and $\Delta G°$ is the driving force. Graphical analysis of the experimental data (**Figure 10c**) suggested that the observed k_{CT} value can be obtained from three sets of parameters, meaning that equation 5 has three solutions that could give rise to the observed rate constants (the black dots in **Figure 10c**): (a) λ_t = 1.2 eV, β = 1.25; (b) λ_t =1.75 eV, β = 1. 5; and (c) λ_t = 2.35 eV, β = 1.75. The physical interpretation of these parameters suggests that the λ_t of 2.35 eV (set c) represents considerable structural reorganization that is not likely to occur in the confined octahedral cavities of the MOF, whereas the parameter sets (a) and (b) can be feasible and precedented in CT process between porphyrins with fixed intermolecular distance.

Being an excellent electron acceptor, C$_{60}$ has been infiltrated into the pores of MOFs as an approach to induce photo/electrical conductivity. Goswami *et al.* have reported that the conductivity of TBAPy based Zr-MOF NU-901 can be increased substantially upon C$_{60}$ incorporation due to a strong electronic interaction at the ground-state leading to an ET from the pyrene-based linker to C$_{60}$.[85] The Cramer group computationally studied PCT between C$_{60}$ and two porphyrin-
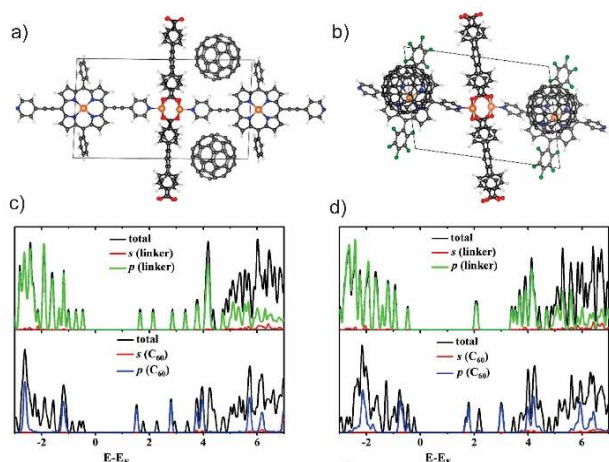
Figure 11. Optimized crystal structures of a) C_{60}@DA-MOF; b) C_{60}@F-MOF; Calculated density of states for c) DA-MOF and (d) F-MOF before (upper panel) and after (lower panel) C_{60} incorporation. The energy is relative to the Fermi level, and the y axis for the s- and p-orbitals is scaled by a factor of 1.75. Reproduced with permission from ref. 117. Copyright 2020, American Chemical Society.

based pillar-paddlewheel MOFs:[117] Zn$_2$(TCPB)(DA-ZnP) denoted as DA-MOF (TCPB = 1,2,4,5-tetrakis(4-carboxyphenyl)benzene, DA-ZnP = [5,15-bis[(4-pyridyl)ethynyl]-10,20-diphenylporphinato]zinc(II); **Figure 11a**) and Zn$_2$(TCPB)(F-ZnP) (*i.e.* denoted as F-MOF; F-ZnP = [5,15-di(4-pyridyl)-10,20-bis(pentafluorophenyl)porphinato]-zinc(II); **Figure 11b**). Calculated optical band gaps for DA-MOF and F-MOF are 1.66 and 2.04 eV, respectively. After C_{60} infiltration, the C_{60}@DA-MOF (**Figure 11c**, lower panels) and C_{60}@F-MOF (**Figure 11d**, lower panels) show band gaps that are 0.16 and 0.36 eV lower than their respective pristine DA-MOF and F-MOF. Partial density of states (PDOS) of C_{60} infiltrated MOFs reveals that the HOCO mainly comprises p-orbitals of the porphyrin linkers and the LUCO predominantly comprises p-orbitals of C_{60}. The significant orbital overlap between orbital of C_{60} and MOF linkers indicates that photoelectrons or holes can be generated on the linker should readily transfer to C_{60} at the interfacial region. This study theoretically demonstrated the strategy that the incorporation of electronic complementary moieties into MOF channels, even without covalent bonding to the framework, can alter the electronic properties of MOF composition that may be used for PCT.

III. Applications of PCT in MOF

III. A. MOFs-based Photocatalysis

The key point that we take note from the above discussion is that the compositional versatility possible from the wide choice of photoactive struts, metal nodes, and various post-synthetic strategies may allow the development of functional frameworks that are decorated with a plethora of optical or redox components as well as catalytic species. These inherent design flexibility and molecular scale porosity make MOF as promising

candidates as photocatalysts. Nevertheless, the intrinsic advantages of MOF-based design lie on its ability to achieve high substrate and catalysts concentration within the MOF pores, where PCT between the sensitizer and the catalyst can occur efficiently due to their proximity. Thus, unlike the homogeneous systems, photocatalysis in MOF is not limited by the diffusion of the catalyst species to the sensitizer, rather the diffusion of the substrate and product. As such, light-driven reactions can be divided mainly into two categories: first, where a sensitizer drives chemical reactions only by EnT process, like the triplet EnT to drive a C-C bond formation (e.g. cycloaddition reaction) as well as reactive oxygen generation that carries out oxidation reaction of, for example, mustard gas simulant. The other photocatalysis involves PCT, where one of the photo-generated charge is used to drive single or multi-electron redox reactions. Here, we focus on the second category, *i.e.* MOF-based photocatalysis that involves PCT. In such reactions, sacrificial reagents are involved to irreversibly regenerate the photosensitizers after every turnover. Sensitized chemical reactions,[118] and those driven *via* generation of singlet oxygen by MOFs[119-122] do not involve PCT and are excluded from the following discussion.
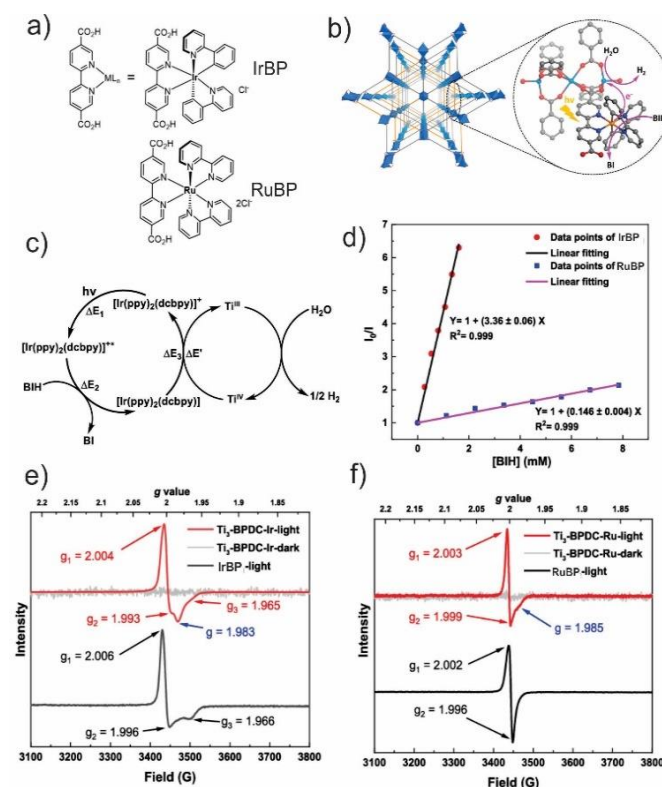
Figure 12. a) Synthesis of Ti$_3$-BPDC-Ir and Ti$_3$-BPDC-Ru; b) schematic showing electron injection from photoreduced ligands in [Ir^{III}(ppy)$_2$(dcbpy$^{-•}$)]^0 into Ti$_3$(OH)$_2$ SBUs to conduct HER (Ti, Ir, O, and N atoms are shown in blue, gold, red, and mazarine, respectively). c) Proposed Ti$_3$-BPDC-Ir catalytic cycle for the light-driven HER, depicting the valence exchange Ti^{III}/Ti^{IV} formed through PCT; d) Stern Volmer plots of I$_0$/I for RuBP and IrBP as a function of the concentration of BIH (mM) regenerator. The EPR spectra of (e) Ti$_3$-BPDC-Ir and (f) Ti$_3$-BPDC-Ru are shown in the dark or under light irradiation. Reproduced with permission from ref. 125. Copyright 2019, American Chemical Society.

Transition metals can activate small molecules (e.g. H_2O and CO_2) by selective binding and therefore can be used as catalytic sites for energy conversion reactions like hydrogen evolution reaction (HER) or CO_2 reduction reaction (CRR). The study of HER process catalytically driven by TiO_2 and titanium-oxo clusters have revealed that a photosensitized CT plays a critical role in high turnover despite its inherent semiconducting nature because TiO_2 is a large-bandgap material corresponding to UV-light ($\lesssim$ 400 nm) and less effective to the solar spectrum. The photosensitizer absorbs photons at the visible region of the solar spectrum to drive PCT to the TiO_2 composition if their excited-state oxidation potential lies higher in energy than the TiO_2 conduction band. Following the PCT, the reduced Ti-centers can catalyze HER.[123, 124] The Lin group synthesized two new MOFs, Ti_3-BPDC-Ir and Ti_3-BPDC-Ru (BPDC = biphenyl-4,4'-dicarboxylate) using a mixed linker strategy (**Figure 12a**), where they doped $[Ir(ppy)_2(dcbpy)]^+$ (hereon IrBP) or $[Ru-(bpy)_2(dcbpy)]^{2+}$ (hereon RuBP) (ppy = 2-phenylpyridine, bpy = 2,2'-bipyridine, and dcbpy = 4,4'-dicarboxy-2,2'-bipyridine) photosensitizers into the Ti_3-BPDC framework which also serves as catalysts for HER (**Figure 12b**).[125] In these studies, 1,3-dimethyl-2-phenyl-2,3-dihydro-1H-benzo[d]imidazole (BIH) was employed as sacrificial regenerator (electrons supplier). To investigate whether the excited photosensitizer was reductively quenched by BIH or oxidatively quenched by $Ti_3(OH)_2$ SBUs, a luminescent quenching experiment for IrBP and RuBP was conducted separately in a homogeneous solution in presence of BIH or the SBU-equivalent model $Ti_6O_6(OiPr)_6(abz)_6$. The spectroscopic data (**Figure 12d**) show that the luminescence of IrBP and RuBP was efficiently quenched by BIH but not by the titanium cluster. This quenching experiment suggests that, in MOF, the CT proceeds from BIH to the excited IrBP or RuBP forming the reduced IrBP or RuBP species that finally transfer the charge to the Ti-center; the final reduced Ti^{III} is evinced by EPR signal (**Figure 12e, f**). The reduced titanium SBU, Ti^{IV}/Ti^{III}, is responsible for HER activity. As demonstrated by DFT calculation, this multi-electron LMCT process involves the formation of Ti^{IV}-H intermediate, the rate-determining step with an energy barrier of 0.76 eV in a proton-coupled ET process. The protonation of Ti^{IV} hydride produces H_2 and regenerates the $Ti^{IV}_3(OH)_2$ cluster (**Figure 12c**).

In a similar photosensitizer-based design, Yan *et al.* studied MOF-based PCT involving $Ru(phen)_3$-derived strut (hereon RuPhen) and Eu^{III} based SBU. The reduced binuclear Eu^{II}_2 clusters, generated by excited RuPhen *via* PCT, serve as catalytic centers for the selective reduction of CO_2 into formate in a two-electron process (**Figure 13a**).[126] The PCT process in Eu-$Ru(phen)_3$-MOF was probed *via* fs-TA spectroscopy (**Figure 13c**). In contrast to free RuPhen, the ultrafast pump-probe data of the MOF reflects a significant reduction of the ESA amplitude. Excited-state dynamical data (**Figure 13d**) suggested a faster ESA decay kinetics of the MOF probed at 604 nm compared to the free RuPhen. This faster decay was postulated to the PCT from the T_1 state of RuPhen species to the Eu clusters. For the catalytic pathway, the authors investigated if the quenching of RuPhen* proceeds by TEOA reductively or an oxidative quenching by Eu_2 clusters occurs first. For that, luminescence
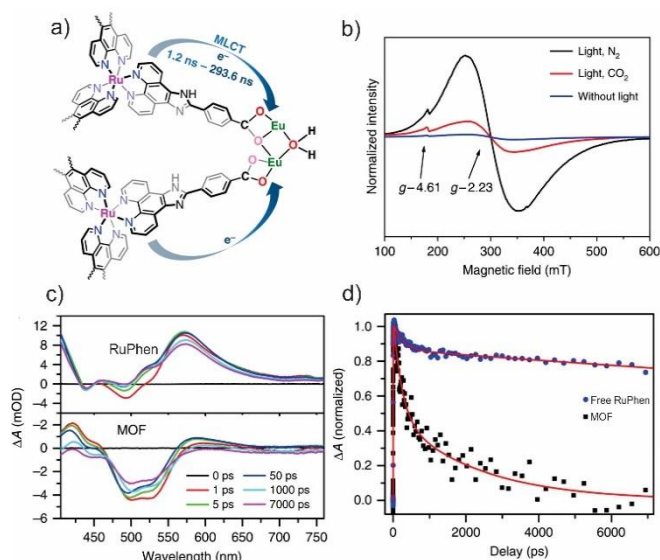

Figure 13. a) Schematic showing PET of Eu-$Ru(phen)_3$-MOF based on the initial excitation of the Ru photocenter and the pathways of ET from Ru to catalytic Eu_2 oxo-cluster center. b) In situ EPR spectra of Eu-$Ru(phen)_3$-MOF under different conditions; c) fs-TA spectra of Eu-$Ru(phen)_3$-MOF and H_3L at various time delays at 604 nm; d) Kinetic profile of species traced at 604 nm in free RuPhen and Eu-$Ru(phen)3$-MOF. Reproduced with permission from ref. 126. Copyright 2018, Nature Publish Group.

quenching experiments of free RuPhen were carried out in a DMF-solvated form with the addition of TEOA or Eu_2 clusters, separately. A significant quenching by Eu_2 clusters was observed rather than the TEOA; this finding reflects an oxidative CT from RuPhen* to the low-lying orbitals of the Eu^{III}_2 clusters as a viable route. This oxidative PCT involving the metal SBU is different from the reductive PCT with the sacrificial reagent observed in Lin's work. The two EPR signals (**Figure 13b**) of the Eu-$Ru(phen)_3$-MOF with g=2.23 and 4.16 revealed the existence of paramagnetic Eu^{2+} species derived from the one-electron reduction of Eu^{3+} that has no EPR response. While the authors did not present any further spectral evidence, their DFT computations suggest that the photocatalytic process involves an exposed Eu^{III} site that adsorbs one CO_2 *via* Eu-O binding. The reduction of CO_2-Eu intermediate can be efficiently driven by the PCT with an impressive rate of 321.9 μmol h^{-1} mmol MOF^{-1}.

Both Lin and Yan's works employed noble-metal (*i.e.* Ir or Ru)-based complexes as photosensitizer with different metal SBUs serving as the catalytic center – their choices depend on the targeted reactions (*i.e.* HER or CO_2 reduction as the driving potentials for these transformations are different). It is interesting to note that the PCT sequence in two different MOFs occurred through different pathways, from the excited sensitizer, one involved ET to the node, and the other involved a hole transfer to the redox regenerator. Such a mechanistic difference often stems from the difference in the rate. The factors that play a critical role in determining the rate include the thermodynamic driving force, reorganization energy, and electronic coupling. The underlying reason may arise from the difference in the electronic properties of metal nodes and sacrificial reagent including their redox potential. Considering the charge carrier states are mere localized, redox potential

measured for the MOFs often represents the frontier orbitals of the monomeric species. For example, the electrochemical data presented in Lin's work suggest that the HOCO (the IrBP centered oxidation) is at 1.49 V, which lies 1.16 V more positive than the BIH$^+$/BIH potential (0.33 V). In contrast, the Ti^{IV}-OH/Ti^{III}-OH (ca -0.63V) lies only ~0.1V positive than the LUCO of this photosensitizer MOF (-0.72 V).[125] This can also be visualized from the excited-state redox potentials of a related IrBP compound, where the E_{ox}^{Ir*} = -0.61 V (vs NHE; reported value of -0.85 V vs SCE)[127] and that should not provide much driving force for PCT to the Ti^{IV}-OH/Ti^{III}-OH (ca -0.63 V). Alternatively, E_{red}^{Ir*} = +0.92 V, which is significantly positive than the BIH$^+$/BIH potential (0.33 V). It is interesting to note that excited IrBP* sensitizers are well known to get reductively quenched (by a sacrificial reagent) to generate a strong IrBP$^-$ reductant.[128-130] For Yan's Eu-Ru(phen)$_3$-MOF, the potential energy difference between E_{ox}^{Ru*} (= − 0.72 V vs NHE; determined by subtracting the emission energy of 2.07 eV (i.e. E_{00} at 598 nm maxima) from the oxidation potential of 1.35 V)[126, 127] and the conduction band of Eu$_2$O$_3$ (-0.68 V) is sufficient enough to drive the PCT from RuPhen* to Eu-SBU. In contrast, E_{red}^{Ru*} = +0.78 V (vs NHE; determined by adding 2.07 eV of E_{00} to the reduction potential of -1.29 V) renders not much potential energy difference with TEOA$^+$/TEOA (ca 0.81-1.07 V)[131-133] to drive a spontaneous PCT. While these energetics measured for their corresponding models in homogeneous solution explains the trend, one should recognize that the adopted regional geometry, close spatial separation between the exact complementary pairs might be different in MOF to facilitate PCT more efficiently (or less) than predicted in homogeneous solution (or solvent-dispersed) systems.

Using Ru(bpy)$_3$$^{2+}$ derivative as the photosensitizer, Lin and coworkers assembled a related longer analog, bis(2,2'-bipyridine)[5,5'-di(4-carboxyl-phenyl)-2,2'-bipyridine]ruthenium(II) dichloride (hereon RuBPP) together with Hf$_{12}$ SBUs to form a 3D framework denoted as Hf$_{12}$-Ru.[134]
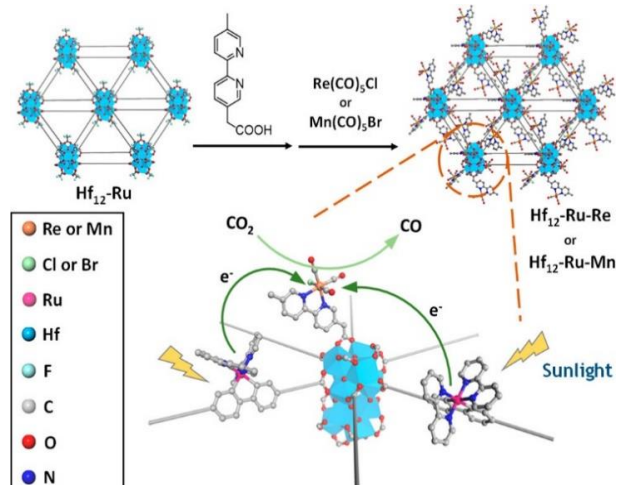
Figure 14. Schematic illustration of the synthesis of Hf$_{12}$-Ru-M (M = Re or Mn) via monocarboxylic acid exchange of Hf$_{12}$-Ru and sunlight-driven CO$_2$ reduction through a mechanism of PET from RuBPP* to M^I(bpy)(CO)$_3$X (M = Re, Mn) that serves as catalytic sites binding with CO$_2$. Reproduced with permission from ref. 134. Copyright 2018, American Chemical Society.

Postsynthesis method was employed to install a secondary carboxy-appended bipyridine complex, M^I(MeMBA)(CO)$_3$X (M = Re, Mn; MeMBA = methyl 2-(5'-methyl-[2,2'-bipyridin]-5-yl)acetate), onto the Hf$_{12}$ SBUs. This SALI-like functionalization fixes the key components in the proximity (distance between the RuBPP photosensitizer strut and the adjacent M^I(bpy)(CO)$_3$X catalysts is ca 13 Å) to efficiently drive PCT. Note that this class of organometallic compounds are well-established homogeneous catalysts that bind CO$_2$ and drive photocatalytic production of CO (98% selectivity) by accepting an electron from the RuBPP* photosensitizers (**Figure 14**).[135-137] While no direct spectroscopic evidence was provided, the authors, in a separate homogeneous quenching test with the model components of Hf$_{12}$-Ru MOF, found that the phosphorescence of the RuBPP strut got more efficiently quenched by the sacrificial BIH regenerator than the electron acceptor M^I(bpy)(CO)$_3$X. It is therefore presumed that the reduced [Hf$_{12}$-Ru]$^-$species, produced from a reductive PCT by BIH, is responsible to prepare the active form of M^I(bpy)(CO)$_3$X for CO$_2$ reduction. The authors further reasoned that the first reduction potential of the RuBPP component (-0.65 V vs NHE) is sufficiently reductive than the LUMO of the Re(MeMBA)(CO)$_3$Cl (0.10 V) to convert its active form. However, the PCT here involved *RuBPP and the BIH; the E_{red}^{RuBPP*} ≃ +0.92 V[127] is significantly positive than the BIH$^+$/BIH potential (0.33 V)[125, 138] to drive the PCT.
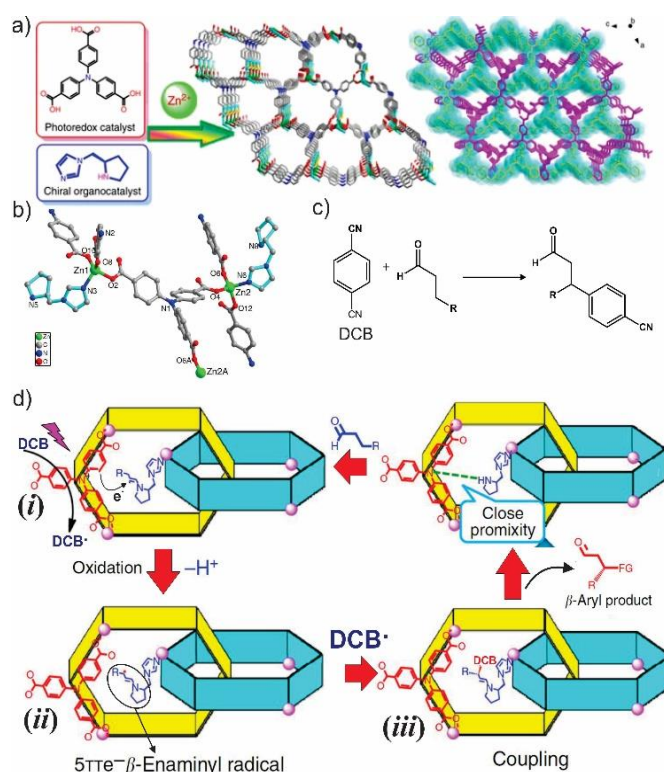
Figure 15. a) Chemical structures of the interpenetrated InP-1 MOF and its components; b) Coordination environments of the Zn(II) ions and NTB^{3-} linker; c) The net β-arylation reaction of saturated aldehydes; d) Proposed mechanisms for interpenetrated MOFs in photocatalytic β-carbonyl activation, showing the PCT pathway and the formation of radical intermediates. Reproduced with permission from ref. 139. Copyright 2017, Nature Publish Group.

An interesting concept of organic transformation involving C-C bond formation was reported by the Duan group using a hybrid crystalline framework (named InP-1). The InP-1 MOF was constructed from L-pyrrolidin-2-ylimidazole (L-PYI, a chiral organocatalyst) and 4,4′,4′′-nitrilotrisbenzoicacid (H₃NTB, photosensitizer)[139] with a twofold interpenetrated framework structure (**Figure 15a**), where the L-PYI and H₃NTB components are proximally arranged in space (**Figure 15b**). Within each of the identically isolated chiral framework, the Zn(II) ions at the node were coordinated in a chiral tetrahedral geometry with three carboxylate oxygen atoms from three different NTB³⁻ linkers and one nitrogen atom from the L-PYI co-ligand. The photocatalyst exhibits excellent activity for the β-arylation of aldehyde derivatives (**Figure 15c**). The photocatalytic process starts with the H₃NTB* photosensitizer that reduces one of the reactant 1,4-dicyanobenzene (DCB) into a radical form DCB•⁻ *via* PCT (**Figure 15d** (i)). The resulting NTB•⁺ is then quickly regenerated/reduced by the enamine intermediate that is bound to L-PYI forming an enaminyl radical cation (**Figure 15d** (ii)), which then reacts with the DCB•⁻. Here, the electron acceptor in the PCT and the regenerator both are reactants of the catalytic conversion, where a cascade consists of PCT followed by CT events is facilitated by the proximity of the key components L-PYI and H₃NTB (**Figure 15b**). The PCT from H₃NTB* to DCB is probed by the luminescent quenching experiment showing a lifetime drop of H₃NTB from 4.62 to 3.25 ns.

III.B. Photoelectrochemical processes in MOFs

MOFs can be an ideal platform for facile PCT and related processes; recalling that the chromophore assemblies in MOFs exert antenna behavior, the D/A ratio as well as the concentration of the catalyst moieties also can be widely varied. However, a photocatalytic activity would require an equivalent amount of redox quencher to regenerate the sensitizer. Instead, the excitons can be delivered to a catalytic center or external electrical contacts, where the charge-carrier generation can be spontaneously driven by the local potential difference. The short-lived excited states and the rapid recombination of the charge carriers seem to be major challenging factors for utilizing the photo-generated redox equivalents (i.e. charge with appropriate potential) and hence a limited catalytic efficiency is achieved. In a photoelectrochemical process, the opposite (residual) charges also need to be transported either for catalytic utilization or to be collected at the external electrical contact. Because common metal-carboxylate (or metal/N-base) connectivity manifest charge carriers that are localized either at the linkers or at the metal node, the charge transport in MOF involves a hopping. Literature reporting on charge hopping indicates that the process is diffusion limited by the counter ion.[53, 140-143] However, when multiple redox steps are necessary to obtain the active form of the catalysts MOF-incorporated sensitizer (light-harvester) and catalyst assembly guarantees to circumvent major mass-transport related problems. Within MOF based sensitizer-catalysts assemblies, each of the intermediates formed during the progressive transformation of
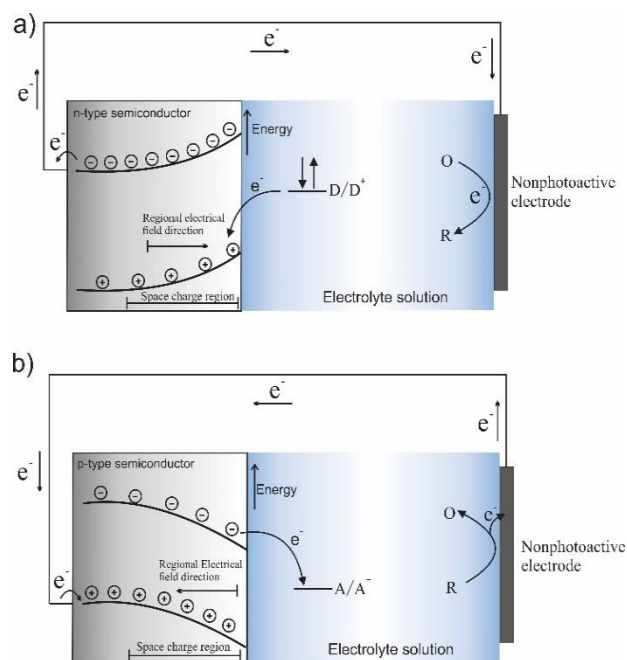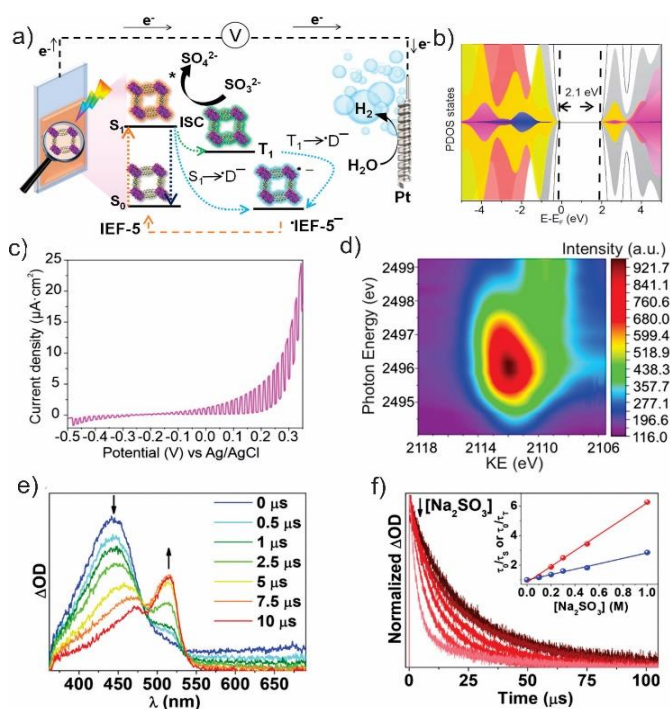

Figure 16. Scheme of a) n-Type and b) p-Type semiconductor cell, depicting the formation of space chare region, locally bending of bands under irradiation and the direction of electron flow. The interfacial electron transfer between the photoelectrode and D/D⁺ or A/A⁻ species in solution are illustrated too.

the resting assembly into an active one would not be susceptible to (a) unwanted diffusion away from a photo-electrode and back into bulk solution, (b) deactivation due to chemically irreversible encounter, and (c) physical loss of inadequate solubility and therefore precipitation of the intermediate species. Within a solid assembly, the separation of electron-hole pair can be promoted by the electrical field that is either spontaneously formed at the interface of the photoelectrode or by an external electrical field to direct electrons and holes to participate in reduction and oxidation reactions before they recombine (**Figure 16**).[144-147] In classic semiconducting band picture, when the *n*-type semiconductor is employed as the photoelectrode, electrons and holes are formed at the surface by splitting the photo-generated excitons at the surface; the electrons are locally driven to the interior bulk whereas holes to the surface, which spontaneously forms a local electrical field –a phenomenon represented by the band bending (**Figure 16a**).[148] Likewise, the *p*-type semiconductor (**Figure 16b**) forms a regional electrical field pointing toward the opposite direction as the n-semiconductor case. The picture in MOF, however, is not this simple and universal. Even for a sluggish hopping-mediated charge transport process, charge that is hopping within MOF crystals deposited on a semiconducting electrode surface (*e.g.* a MOF modified TiO₂-layered-FTO electrode) would feel a similar force field (stemming from the potential energy difference between the semiconductor band edge and the concerned MOF redox potentials) driving a directional transport. Alternatively, exciton splitting can be achieved under an applied bias voltage over the circuit to steer the photogenerated electrons or holes –in such

cases, no semiconducting layer is used (*e.g.* MOF modified FTO electrode).[37]

García-Sánchez *et. al.* synthesized a new MOF, IEF-5, with bismuth and dithieno[3,2-b:2',3'-d]thiophene-2,6-dicarboxylic acid (DTTDC). They constructed their photoanode by depositing the IEF-5 on ITO; the photoelectrons collected were used to drive HER at the Pt counter electrode (**Figure 17a**).[149] Computational work on PDOS revealed that the IEF-5 has 2.1 eV bandgap (**Figure 17b**). The positive response of the photocurrent (**Figure 17c**) indicates an n-type semiconductor. Prior to charge separation, photoexcitation leads to an ultrafast charge redistribution defined by an electron delocalization around sulfur atoms. This process was probed *via* synchrotron Core Hole Clock (CHC) experiments (**Figure 17d**), which involves recording the S KLL Auger spectra at different excitation energies around the sulfur K-edge with attosecond time resolution. The charge delocalization time was calculated as 1.27 fs. The optical TA spectra collected for IEF-5 with a 355 nm pump/white-probe setup exhibit a band at 440 nm with a first-order decay (τ =25 μs; **Figure 17e**) and was attributed to a possible transient absorption in the triplet manifold.

In the presence of a redox quencher such as an electron donor Na_2SO_3 ($E^0_{SO_3^{2-}/SO_4^{2-}}$ = 0.93 V vs NHE) in the solution, pump-probe experiment displayed TA spectra that highlight quenching of the 440nm band and evolution of new 515 nm transition due to the formation of radical anion IEF-5$^{\bullet-}$ upon PCT. The PCT can be described as a reductive quenching of the MOF excited state by the SO_3^{2-}. Interestingly, the IEF-5$^{\bullet-}$ the signal was no longer detected in an oxygen-saturated solution. The oxygen quenching experiment suggests the PCT involves ^{3}IEF-5*. The relative contribution of ^{1}IEF-5* and ^{3}IEF-5* species in the PCT process was determined by a Stern–Volmer analysis. With the $K_{SV(S)}$ of 1.85 and 5.35 M^{-1} for singlet and triplet excited-states, respectively, the authors suggested that the ^{3}IEF-5* is the key driver of the PCT. The photogenerated electrons are transported to the counter electrode performing HER; a constant H_2 evolution was observed with a 2.35 μmol cm^{-2} gas accumulated within 60 minutes of irradiation.

Morris and coworkers incorporated mixed-linkers including a RuBP photosensitizer and catalytic site [Ru(tpy)(dcbpy)Cl]$^+$ (hereon RuTB; tpy = 2,2':6',2''-terpyridine) into UiO-67 MOF as a photoelectrode material (**Figure 18a**).[150] A thin MOF film was
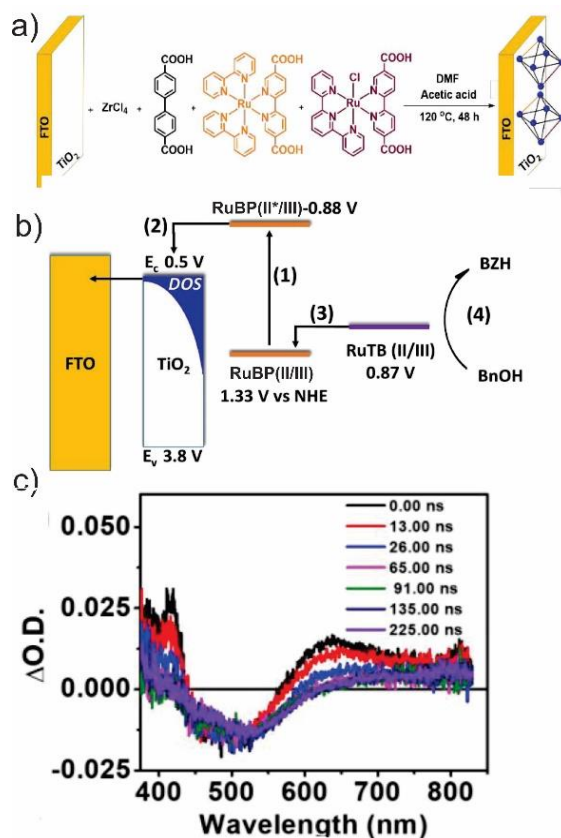

Figure 17. a) Scheme of MOF-based photoelectrochemistry cell for HER, highlighting the ET through singlet and triplet states; b) Atom-projected partial density of states (PDOS) for Bi 2s (magenta), Bi 2p (blue), C 2p (gray), sulfur (yellow), oxygen (red); c) LSV under chopped illumination showing the photocurrent density at different bias potentials; d) 2D core hole clock measurements of IEF-5; e) TA spectra acquired at different delay time under the excitation of 355 nm for IEF-5 in presence of Na_2SO_3 as electron donor. f) Evolving of the triplet lifetime (λ_{ex} = 355 nm) as the function of concentrations of Na_2SO_3. The inset is Stern–Volmer plot for singlet (blue) and triplet (red). Reproduced with permission from ref. 149. Copyright 2020, American Chemical Society.

Figure 18. a) Schematic representation of MOF/TiO$_2$/FTO assembly via a direct solvothermal synthesis of the mixed-linker MOF film; b) Energy diagram illustrating the photophysical process at the photoelectrode, including (*i*) photoexcitation of Ru^{II}BP to Ru^{II}BP*; (*ii*) electron injection from Ru^{II}BP* into the conduction band of TiO$_2$; (*iii*) oxidation of Ru^{II}TB by Ru^{II}BP to form Ru^{III}TB; and (*iv*) oxidation of benzyl alcohol (BnOH) by Ru^{III}TB to benzaldehyde (BZH); c) ns-TA spectra of RuBP-RuTB-UiO-67-TiO$_2$/FTO. Reproduced with permission from ref. 150. Copyright 2020, Royal Society of Chemistry

grown on an n-type semiconducting (TiO$_2$-coated FTO) electrode serving as a photoanode for the oxidation of alcohol. The proposed mechanism in **Figure 18b** shows that electrons are injected to TiO$_2$ layer from the Ru^{II}BP*, thereby generating a hole that forms Ru^{III}BP. The Ru^{II}TB is subsequently oxidized by Ru^{III}BP forming Ru^{III}TB that finally oxidizes alcohol. This photophysical pathway is demonstrated by the ns-TA spectra, which highlight that the excited state absorption band of RuBP-RuTB-UiO-67-TiO$_2$/FTO near 420 nm diminishes significantly (**Figure 18c**); this was attributed to the charge injection from Ru^{II}BP* to the conduction band of TiO$_2$. The authors observed that the isosbestic point (at ΔO.D. = 0) exhibits a bathochromic shift from 555 to 620 nm over time (**Figure 18c, d**) due to a delayed formation of Ru^{II}TB* or Ru^{III}TB, which could happen in one of the two ways: either the formation of Ru^{II}TB* is occurring *via* EnT from RuBP* to Ru^{II}TB; alternatively, Ru^{III}TB could be formed *via* oxidation by Ru^{III}BP that was formed upon PCT (to TiO$_2$, **Figure 18b**, step 3). The time-constant (21.0 ± 0.3 ns) for the shift of the isosbestic point was determined from the delayed growth at 550 nm. Based on these experimental data, it seems neither pathway could be ruled out -although the authors preferentially proposed the second process as a dominating route. For such a system, varying the ratio of the primary photosensitizer and the catalysts and/or a solvent-dependent transient spectroscopic measurement may provide further information regarding the preferentially adopted photophysical pathway.

As discussed above, MOFs can be used as dye assembly and can be deposited on a transparent conducting electrode (TCO) such as FTO or ITO. To make the MOF-modified electrode (i.e. MOF film deposited/grown on TCO) serving as photocathode or photoanode, commonly p-type (e.g., NiO) or n-type (e.g. TiO$_2$) large bandgap semiconducting layers are deposited as a barrier (i.e. in between the MOF layer and TCO). These semiconducting layers not only facilitate exciton splitting at their interfaces with the dye (here MOF) but also provide an augmented connection that provides charge-carrier doping based on their potential and therefore collects the electron or hole. In contrast, by

switching the redox mediator (D or A species) in the electrolyte, the MOF-based photoelectrode can be made to serve as a photoanode or photocathode accordingly. Such fabrication is different from a standard semiconducting layered electrode because, for the MOF-only system, the kinetic of PCT at the MOF-electrolyte interface dictates the polarity of the MOF-modified electrode. Hod and coworkers demonstrated that the interfacial CT kinetics at the surface of porphyrin-based MOF-525/FTO photoelectrode could be tuned by introducing electron or hole-accepting species, such as water and triethanolamine (TEOA) into the electrolyte solution (**Figure 19a, b**).[37] The introduction of a hole-acceptor TEOA displayed a photo-anodic response: *i.e.* under light illumination, a positive increment of current density was observed with a shift of the onset oxidation potential from 0.85 V to 0 V (*vs* NHE; **Figure 19c**). In the case of water as the electron acceptor, photo-cathodic
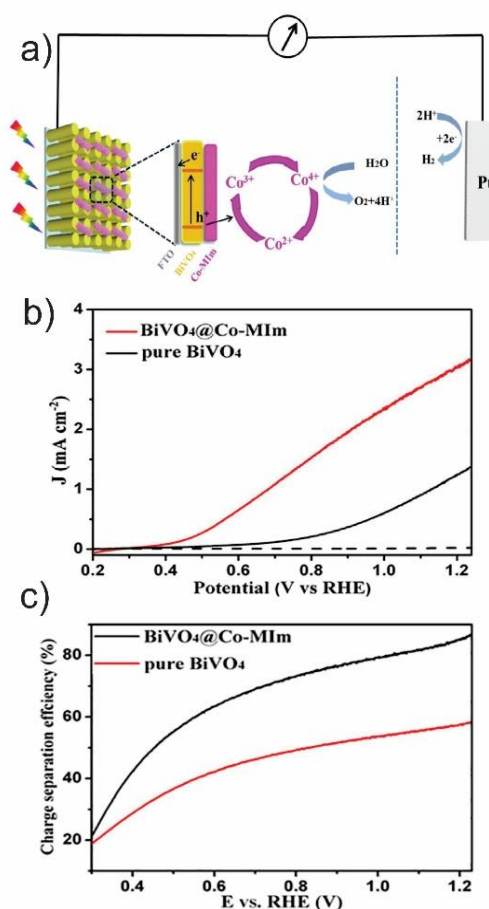
Figure 20. The proposed photogenerated charges generation, transport, and water splitting reaction on the BiVO4@Co-MIm anode; b) LSV curves of BiVO4 and BiVO4@Co-MIm electrodes under illumination, the dotted line is LSV curve of BiVO4@Co-MIm without illumination for comparison; c) Charge separation efficiency of BiVO4 and BiVO4@Co-MIm electrodes at different potentials. Reproduced with permission from ref. 151. Copyright 2019, Elsevier.

Figure 19. a) The components for MOF-525 assembly and the fabrication of photoelectrode; b) scheme illustration of the PET in photoanode and photocathode fabricated by MOF-525, in the presence of TEOA as D or H$_2$O as A respectively; LSV curves for MOF-525 c) photoanode (i.e. TEOA in solution as donor species) and d) photocathode (i.e. H$_2$O as electron acceptor) in the dark (black) and under light (red). Reproduced with permission from ref. 37. Copyright 2019, Royal Society of Chemistry.

behavior was observed upon light illumination, where electrons from the excited MOFs are transferred to protons generating H$_2$. In the latter case, dark and light LSV measurements exhibit an increasing current density in a negative direction (**Figure 19d**), attributed to the PCT from MOF-525* to water. Photo induced oxidation of TEOA to TEOA$^{•+}$ is a fast one-electron process,

whereas photo induced reduction of water to H_2 at photocathode is relatively and kinetically sluggish 2-electron process. Hence, the photo generated charges spend a longer time in photocathode, simply increasing its probability to recombine *via* for example, solution charge accepting species.

Zhou *et al.* fabricated a bismuth vanadate electrode covered with porous cobalt and imidazole 'Co-Mim' (Mim = 2-methylimidazole, this Co-Mim is structurally different from ZIF-67) and used this photoanode for water oxidation.[151] At 1.23 V (*vs* RHE) BiVO$_4$@Co-MIm electrode shows 2.4 times more photocurrent compared to the bare $BiVO_4$ electrode (**Figure 20b**). The plot of the photogenerated charge separation efficiency (Φ_{sep}) as a function of applied potential suggests that BiVO$_4$@Co-MIm exhibits higher Φ_{sep} compared to the pristine $BiVO_4$ in the entire range (**Figure 20c**). Here, $\Phi_{sep} = J_{sep} / J_{abs}$; where J_{sep} is the current density measured in the electrolyte containing hole trapping agent (Na_2SO_3) and J_{abs} is the maximum theoretical current density. The author suggests that the cobalt ion suppresses the recombination of the holes reaching the surface; thus, promoting hole injection to the electrolyte by creating an energy barrier for the hole to recombine. **Figure 20a** shows the proposed mechanism of water oxidation. Under light illumination, $BiVO_4$ would be excited to produce the photogenerated electron-hole pairs, where the hole transfer to the Co-Mim layers to generate Co^{3+} and then Co^{4+} -the active form of the catalysts driving the water oxidation. The OER reaction converts the Co^{4+} back to Co^{2+}. The electrons collected at the photoanode from the reduced $BiVO_4$ are transported to the Pt counter electrode to drive HER. It is intriguing to note that the aligned $BiVO_4$ nanostructures have a large surface area with micrometer-scale pores; the Co-MIm is solvothermally grown at the surface of the $BiVO_4$ nanostructure; thus, the separated charges may not necessarily need to travel significant distances. Furthermore, the deposited Co-MIm component does not seem to contribute to the visible light absorption possibly due to its thin layer morphology. Even though this study specifically did not provide much spectroscopic evidence, the improvement in the photocurrent indicates the involvement of the porous Co-MIM as the hole transport layer through PCT. This design may inspire further development of the MOF based OER system in conjunction with molecular (RuBP, RuPhen, IrBP, etc.) or desired metal-oxide sensitizers.

III.C. MOFs-based Luminescent Sensing

MOFs have been explored as working compositions for sensing applications due to the tunable luminescent properties originating from the linkers and their interaction with secondary species including metallic nodes and guest species.[27, 152-158] The attractive feature in these frameworks is the arrays of binding sites available for the analytes. These binding sites can be installed post-synthetically if not present in the pristine form. The fluorophore/luminophore in MOFs undergoes radiative recombination decay from the excited state (i.e. L*), which gets quenched when the L* gets involved in a PCT reaction. Thus, the extent of the emission quenching in MOFs can be a function of

analyte concentration.[27, 159] These turn-off sensors are common and maybe less selective since it can be susceptible to the introduction of various nonradiative decay pathway, which consequently leads to false reporting.[160] In contrast, turn-on sensors requires selective binding with analytes and therefore, we only focus on the MOF-based systems in which the analytes turn the sensor from non-emissive to emissive form *via* a PCT; note that an EnT based turn-on system is also possible, where the analytes switch off a pre-existing internal D-A based EnT to recover the emission of the D –but we are not discussing those. The Qian group reported ZJU-109 -a cobalt-based mix linker MOF prepared from 2-(4-pyridyl)-terephthalic acid (H$_2$PTA) and 4,4'-bis(imidazolyl)biphenyl (4,4'-bimbp) -which is employed as turn-on sensor for Fe^{3+} ion.[161] Without Fe^{3+}, the PCT proceeds
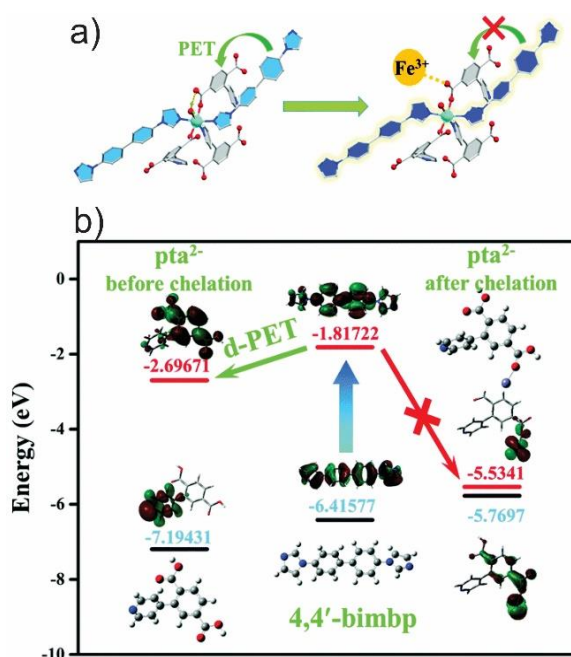
Figure 21. a) Schematic illustration of the PET process and the turn-on sensing of Fe^{3+}; b) Calculated HOMO and LUMO energy levels of 4,40-bimbp and H2PTA pta^{2-} and the PET pathway between the two species. The binding of Fe^{3+} to pta^{2-} energetically hindered PET. Reproduced with permission from ref. 161. Copyright 2019, Royal Society of Chemistry.

from the 4,4'-bimbp* (acting fluorophore) to the PTA acceptor. This efficient PCT precludes the fluorescence of the linker 4,4'-bimbp (**Figure 21a**). With the help of DFT calculation, the authors predicted that that Fe^{3+} binding to PTA^{2-} forms Fe-PTA species with an iron-centered highly stabilized lowest unoccupied orbital (-5.5 eV), which is close in energy to its modified and destabilized valence orbitals (*ca.* -5.8 eV). Thus, the high energy gap from the E_{ox}^{bimbp*} and lowest unoccupied orbital of Fe-PTA attenuates the PCT efficiency (**Figure 21b**). Increase in driving force can effectively reduce the CT-rate if the process is in Markus inverted region (*i.e.* $|\Delta G^0| > \lambda_t$). The authors attributed the recovery of 4,4'-bimbp emission to the blocked ET from 4,4'-bimbp* to Fe-PTA.

Using the mixed-ligand strategy, Gui and coworkers reported the Zr-based UiO-68-An/Ma MOFs with anthracene and maleimide -based mixed linkers as the sensor of biothiols (**Figure 22a**).[162] The low photoluminescence quantum yield (QY

= 1.1%) of UiO-68-An/Ma indicates the fluorescence quenching of anthracene by maleimide through PCT. As shown in the bright-field luminescent images (**Figure 22b**), the QY of UiO-68-An/Ma is recovered to 28.1% when it was exposed to 2-mercaptoethanol that is chemisorbed/trapped with the Ma-component forming UiO-68-An/TE (TE = thiol-ene adduct of the Ma); likewise, a 22.0% QY was observed when exposed to 3-furanmethanol forming UiO-68-An/DA (DA = Diels-Alder product). The binding of 2-mercaptoethanol or 3-furanmethanol onto Ma switched off the PCT from An* to Ma, thus An* could return to the ground state through a radiative process. This special combination of the two chromophores within a framework realizes a tunable PCT by selective binding with the analytes, which enables UiO-68-An/Ma to serve as the sensor for biothiols.
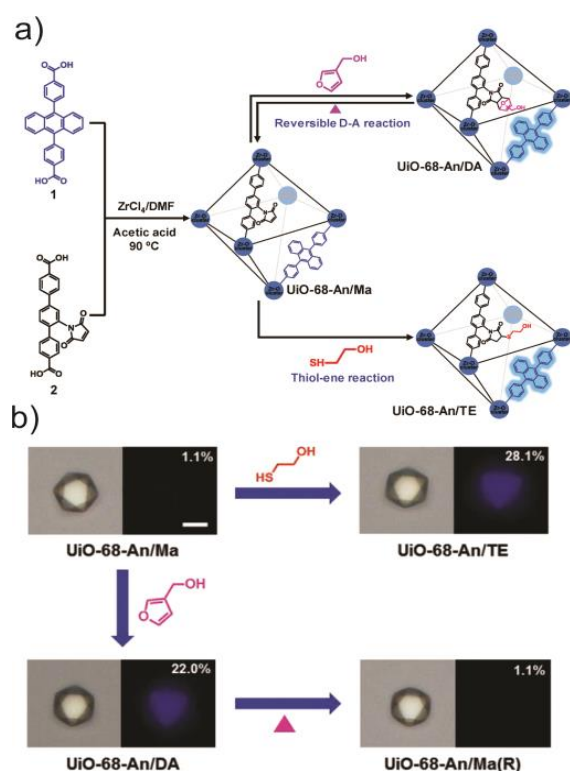
Figure 22. a) Synthesis of UiO-68-An/Ma and tuning the fluorescent PET in the MOF through reversible D–A reaction or thiol-ene reaction; b) Bright-field and photoluminescence images of fresh UiO-68-An/Ma, UiO-68-An/DA, UiO-68-An/Ma(R) excited by mercury lamp, and UiO-68-An/TE. Reproduced with permission from ref. 162. Copyright 2018, Wiley-VCH.

An alternative approach to tune the efficiency of PCT between the chromophores and the neighboring (MOF bound/assembled) quencher can be achieved by knocking out the quenchers *via* a competitive coordination with the analyte. Li et al. synthesized a coordination network that features aggregation-induced emission (AIE) displayed by the assembled hydroxyl-functionalized ligand 4,4'-((Z,Z)-1,4-diphenylbuta-1,3-diene-1,4-diyl)bis(2-hydroxybenzoic acid) (HTABDC) and Zn(II)[163] (Framework 1 = F1). When this zigzag coordination network was combined with 4,4'-bipyridine (Bpy) pillar, it formed a porous 3D network (Framework 2 =F2). However, the AIE of the HTABDC linker, observed in F1, was quenched in F2

by the auxiliary Bpy linker. This quenching was attributed to a facile PCT between HTABDC* and Bpy as the later component has LUMO that lies 1.4 eV lower than that of HTABDC (**Figure 23a**). When this F2 assembly was exposed to Al^{3+} (a specific analyte), the ion gets preferentially chelated by the 2-hydroxycarboxylate moiety of the HTABDC; as a result, the F2 MOF get dissociated (**Figure 23b**). The author claims that F2 dissociation leads to the removal of the Bpy, which, in turn, shuts down the PCT between two types of likers. Thus, the new aggregation of Al-HTABDC recovers of AIE (i.e. the fluorescence is switched on). Interestingly, ~3 ppb (less than the 200-ppb limit set by US-EPA) of Al^{3+} was found sufficient to release enough bpy that AIE recovery was optically (visually) detectable. With these few examples presented above, we can clearly say a superior turn-on sensor can be developed with MOF by suppressing the PCT between internal components as the 'switching off' mechanism upon a selective analyte binding.
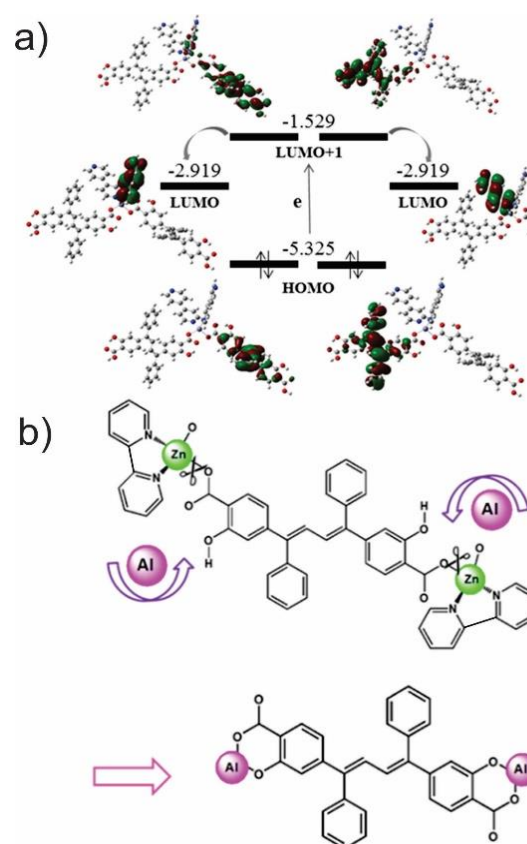
Figure 23. a) Diagram of photoinduced electron transfer from ligands HTABDC to Bpy in Framework 2, indicating a lower LUMO orbital of Bpy than S$_1$ of HTABDC. b) Schematic representation of the competitive coordination between Al^{3+} and Zn^{2+} with HTABDC. Reproduced with permission from ref. 163. Copyright 2018, American Chemical Society.

Conclusion and future perspective

The inherently modular yet precise organization of optoelectronically active species can render a solid compositional platform where PCT can be tuned by virtue of their ground and excited-state potential and distance fixed within the frameworks. Such an organization also offers unique

opportunities to vary the ratio of sensitizer to acceptor or sensitizer to the catalyst, with or without the energy transport bridge. The basic function of MOFs can be versatile, such as sensitizer and light-harvester that can host or incorporate organized molecular interface for charge transfer and subsequent transport for their utilization at a catalytic center or recovery at the external electrical contacts. The precise organization of the desired photoactive species around well-defined pores not only defines the controlled evolution of the photophysical properties but also in a more efficient way, different than what we see in typical molecular aggregates. All these features are key requirements for photocatalysis and photoelectrocatalysis, where understanding the key steps and devising ways to control them can lead to the development of high performing working compositions. Photoinduced charge (both electrons and holes) transfer is only a key middle step here, which requires excitation energy to be efficiently delivered to the exciton splitting interface and the ability after carrying the generated redox equivalents (charge with the appropriate potentials) to the desired place.

Both theoretical and experimental works were presented here to systematically demonstrate the strategy adopted for probing the PCT and its efficient applications. Thus, the appropriate choice of the complementary units and their assembly will define key tools to prolong the exciton lifetime, slow the electron-hole recombination possibly by carrying them far should be part of the future development to improve the photo- and photoelectrocatalytic reactions. For these, one key step is laying the fundamental platform for long-range directional energy and charge transport processes. Once such strategies are adopted in robust MOFs, the system can be diversified with the tailored components for the desired usage. For this, post-synthesis approaches simply widen the horizon of possibilities.

Conflicts of interest

There are no conflicts to declare.

Acknowledgements

Notes and references

‡ Footnotes relating to the main text should appear here. These might include comments relevant to but not central to the matter under discussion, limited experimental and spectral data, and crystallographic data.
§
§§
etc.

1. Long, J. R.; Yaghi, O. M., The Pervasive Chemistry of Metal–Organic Frameworks. *Chem. Soc. Rev.* **2009,** *38* (5), 1213-1214.

2. Zhou, H.-C.; Long, J. R.; Yaghi, O. M., Introduction to Metal–Organic Frameworks. *Chem. Rev.* **2012,** *112* (2), 673-674.

3. O'Keeffe, M.; Yaghi, O. M., Deconstructing the Crystal Structures of Metal–Organic Frameworks and Related Materials into Their Underlying Nets. *Chem. Rev.* **2012,** *112* (2), 675-702.

4. Lu, W.; Wei, Z.; Gu, Z.-Y.; Liu, T.-F.; Park, J.; Park, J.; Tian, J.; Zhang, M.; Zhang, Q.; Gentle Iii, T.; Bosch, M.; Zhou, H.-C., Tuning the Structure and Function of Metal–Organic Frameworks Via Linker Design. *Chem. Soc. Rev.* **2014,** *43* (16), 5561-5593.

5. Bai, Y.; Dou, Y.; Xie, L.-H.; Rutledge, W.; Li, J.-R.; Zhou, H.-C., Zr-Based Metal–Organic Frameworks: Design, Synthesis, Structure, and Applications. *Chem. Soc. Rev.* **2016,** *45* (8), 2327-2367.

6. Li, J.-R.; Ma, Y.; McCarthy, M. C.; Sculley, J.; Yu, J.; Jeong, H.-K.; Balbuena, P. B.; Zhou, H.-C., Carbon Dioxide Capture-Related Gas Adsorption and Separation in Metal-Organic Frameworks. *Coord. Chem. Rev.* **2011,** *255* (15), 1791-1823.

7. Li, J.-R.; Kuppler, R. J.; Zhou, H.-C., Selective Gas Adsorption and Separation in Metal–Organic Frameworks. *Chem. Soc. Rev.* **2009,** *38* (5), 1477-1504.

8. Ma, S.; Zhou, H.-C., Gas Storage in Porous Metal–Organic Frameworks for Clean Energy Applications. *Chem. Commun.* **2010,** *46* (1), 44-53.

9. Murray, L. J.; Dincă, M.; Long, J. R., Hydrogen Storage in Metal–Organic Frameworks. *Chem. Soc. Rev.* **2009,** *38* (5), 1294-1314.

10. Dincă, M.; Long, J. R., Hydrogen Storage in Microporous Metal–Organic Frameworks with Exposed Metal Sites. *Angew. Chem. Int. Ed.* **2008,** *47* (36), 6766-6779.

11. Chen, Z.; Li, P.; Anderson, R.; Wang, X.; Zhang, X.; Robison, L.; Redfern, L. R.; Moribe, S.; Islamoglu, T.; Gómez-Gualdrón, D. A.; Yildirim, T.; Stoddart, J. F.; Farha, O. K., Balancing Volumetric and Gravimetric Uptake in Highly Porous Materials for Clean Energy. *Science* **2020,** *368* (6488), 297-303.

12. Kaur, R.; Kim, K.-H.; Paul, A. K.; Deep, A., Recent Advances in the Photovoltaic Applications of Coordination Polymers and Metal Organic Frameworks. *J. Mater. Chem. A* **2016,** *4* (11), 3991-4002.

13. Lee, D. Y.; Shin, C. Y.; Yoon, S. J.; Lee, H. Y.; Lee, W.; Shrestha, N. K.; Lee, J. K.; Han, S.-H., Enhanced Photovoltaic Performance of Cu-Based Metal-Organic Frameworks Sensitized Solar Cell by Addition of Carbon Nanotubes. *Sci. Rep.* **2014,** *4* (1), 3930.

14. Lee, D. Y.; Shinde, D. V.; Yoon, S. J.; Cho, K. N.; Lee, W.; Shrestha, N. K.; Han, S.-H., Cu-Based Metal–Organic Frameworks for Photovoltaic Application. *J. Phys. Chem. C* **2014,** *118* (30), 16328-16334.

15. Zhang, T.; Lin, W., Metal–Organic Frameworks for Artificial Photosynthesis and Photocatalysis. *Chem. Soc. Rev.* **2014,** *43* (16), 5982-5993.

16. Dhakshinamoorthy, A.; Asiri, A. M.; García, H., Metal–Organic Framework (MOF) Compounds: Photocatalysts for Redox Reactions and Solar Fuel Production. *Angew. Chem. Int. Ed.* **2016,** *55* (18), 5414-5445.

17. Xu, H.-Q.; Hu, J.; Wang, D.; Li, Z.; Zhang, Q.; Luo, Y.; Yu, S.-H.; Jiang, H.-L., Visible-Light Photoreduction of CO_2 in a Metal-Organic Framework: Boosting Electron-Hole Separation Via Electron Trap States. *J. Am. Chem. Soc.* **2015,** *137* (42), 13440-13443.

18. Li, H.; Yang, Y.; He, C.; Zeng, L.; Duan, C., Mixed-Ligand Metal-Organic Framework for Two-Photon Responsive Photocatalytic C-N and C-C Coupling Reactions. *ACS Catal.* **2019,** *9* (1), 422-430.

19. Xiao, J.-D.; Han, L.; Luo, J.; Yu, S.-H.; Jiang, H.-L., Integration of Plasmonic Effects and Schottky Junctions into Metal-Organic Framework Composites: Steering Charge Flow for Enhanced Visible-Light Photocatalysis. *Angew. Chem. Int. Ed.* **2018,** *57* (4), 1103-1107.
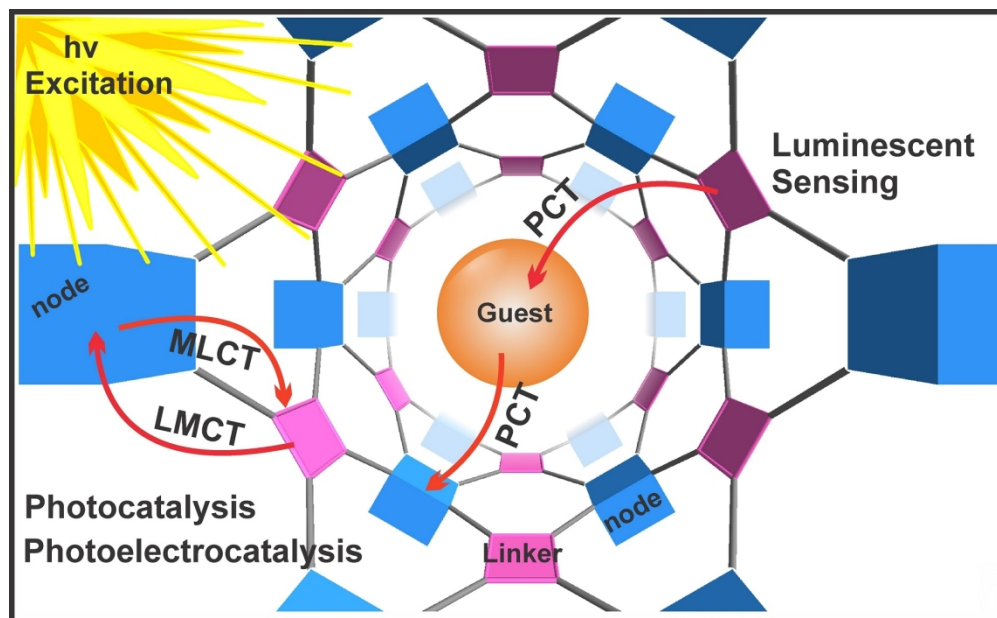
20. Zhang, Y.; Pang, J.; Li, J.; Yang, X.; Feng, M.; Cai, P.; Zhou, H.-C., Visible-Light Harvesting Pyrene-Based Mofs as Efficient Ros Generators. *Chem. Sci.* **2019,** *10* (36), 8455-8460.

21. Wang, C.; Xie, Z.; deKrafft, K. E.; Lin, W., Doping Metal–Organic Frameworks for Water Oxidation, Carbon Dioxide Reduction, and Organic Photocatalysis. *J. Am. Chem. Soc.* **2011,** *133* (34), 13445-13454.

22. Kreno, L. E.; Leong, K.; Farha, O. K.; Allendorf, M.; Van Duyne, R. P.; Hupp, J. T., Metal–Organic Framework Materials as Chemical Sensors. *Chem. Rev.* **2012,** *112* (2), 1105-1125.

23. Cui, Y.; Song, R.; Yu, J.; Liu, M.; Wang, Z.; Wu, C.; Yang, Y.; Wang, Z.; Chen, B.; Qian, G., Dual-Emitting Mof⊃Dye Composite for Ratiometric Temperature Sensing. *Adv. Mater* **2015,** *27* (8), 1420-1425.

24. Zhu, X.; Zheng, H.; Wei, X.; Lin, Z.; Guo, L.; Qiu, B.; Chen, G., Metal–Organic Framework (MOF): A Novel Sensing Platform for Biomolecules. *Chem. Commun.* **2013,** *49* (13), 1276-1278.

25. Gole, B.; Bar, A. K.; Mukherjee, P. S., Fluorescent Metal–Organic Framework for Selective Sensing of Nitroaromatic Explosives. *Chem. Commun.* **2011,** *47* (44), 12137-12139.

26. Yang, S.-P.; Zhao, W.; Hu, P.-P.; Wu, K.-Y.; Jiang, Z.-H.; Bai, L.-P.; Li, M.-M.; Chen, J.-X., Lanthanum-Based Metal-Organic Frameworks for Specific Detection of Sudan Virus Rna Conservative Sequences Down to Single-Base Mismatch. *Inorg. Chem.* **2017,** *56* (24), 14880-14887.

27. Zhu, X.-D.; Zhang, K.; Wang, Y.; Long, W.-W.; Sa, R.-J.; Liu, T.-F.; Lu, J., Fluorescent Metal-Organic Framework (MOF) as a Highly Sensitive and Quickly Responsive Chemical Sensor for the Detection of Antibiotics in Simulated Wastewater. *Inorg. Chem.* **2018,** *57* (3), 1060-1065.

28. Wang, Z.; Cohen, S. M., Postsynthetic Modification of Metal–Organic Frameworks. *Chem. Soc. Rev.* **2009,** *38* (5), 1315-1329.

29. McDonald, T. M.; D'Alessandro, D. M.; Krishna, R.; Long, J. R., Enhanced Carbon Dioxide Capture Upon Incorporation of N,N′-Dimethylethylenediamine in the Metal-Organic Framework Cubttri. *Chem. Sci.* **2011,** *2* (10), 2022-2028.

30. Kim, M.; Cahill, J. F.; Fei, H.; Prather, K. A.; Cohen, S. M., Postsynthetic Ligand and Cation Exchange in Robust Metal–Organic Frameworks. *J. Am. Chem. Soc.* **2012,** *134* (43), 18082-18088.

31. Cohen, S. M., Postsynthetic Methods for the Functionalization of Metal–Organic Frameworks. *Chem. Rev.* **2012,** *112* (2), 970-1000.

32. Li, T.; Kozlowski, M. T.; Doud, E. A.; Blakely, M. N.; Rosi, N. L., Stepwise Ligand Exchange for the Preparation of a Family of Mesoporous MOFs. *J. Am. Chem. Soc.* **2013,** *135* (32), 11688-11691.

33. Karagiaridi, O.; Bury, W.; Mondloch, J. E.; Hupp, J. T.; Farha, O. K., Solvent-Assisted Linker Exchange: An Alternative to the De Novo Synthesis of Unattainable Metal–Organic Frameworks. *Angew. Chem. Int. Ed.* **2014,** *53* (18), 4530-4540.

34. Deria, P.; Mondloch, J. E.; Tylianakis, E.; Ghosh, P.; Bury, W.; Snurr, R. Q.; Hupp, J. T.; Farha, O. K., Perfluoroalkane Functionalization of Nu-1000 Via Solvent-Assisted Ligand Incorporation: Synthesis and CO_2 Adsorption Studies. *J. Am. Chem. Soc.* **2013,** *135* (45), 16801-16804.

35. Deria, P.; Bury, W.; Hupp, J. T.; Farha, O. K., Versatile Functionalization of the Nu-1000 Platform by Solvent-Assisted Ligand Incorporation. *Chem. Commun.* **2014,** *50* (16), 1965-1968.

36. Deria, P.; Chung, Y. G.; Snurr, R. Q.; Hupp, J. T.; Farha, O. K., Water Stabilization of Zr_6-Based Metal–Organic Frameworks Via Solvent-Assisted Ligand Incorporation. *Chem. Sci.* **2015,** *6* (9), 5172-5176.

37. Ifraemov, R.; Shimoni, R.; He, W.; Peng, G.; Hod, I., A Metal–Organic Framework Film with a Switchable Anodic and Cathodic Behaviour in a Photo-Electrochemical Cell. *J. Mater. Chem. A* **2019,** *7* (7), 3046-3053.

38. Yu, J.; Li, X.; Deria, P., Light-Harvesting in Porous Crystalline Compositions: Where We Stand toward Robust Metal-Organic Frameworks. *ACS Sustain. Chem. Eng.* **2019,** *7* (2), 1841-1854.

39. Pattengale, B.; Yang, S.; Ludwig, J.; Huang, Z.; Zhang, X.; Huang, J., Exceptionally Long-Lived Charge Separated State in Zeolitic Imidazolate Framework: Implication for Photocatalytic Applications. *J. Am. Chem. Soc.* **2016,** *138* (26), 8072-8075.

40. Yang, N.-N.; Fang, J.-J.; Sui, Q.; Gao, E.-Q., Incorporating Electron-Deficient Bipyridinium Chromorphores to Make Multiresponsive Metal-Organic Frameworks. *ACS Appl. Mater. Interfaces* **2018,** *10* (3), 2735-2744.

41. Zeng, Y.; Fu, Z.; Chen, H.; Liu, C.; Liao, S.; Dai, J., Photo- and Thermally Induced Coloration of a Crystalline MOF Accompanying Electron Transfer and Long-Lived Charge Separation in a Stable Host-Guest System. *Chem. Commun.* **2012,** *48* (65), 8114-8116.

42. Yamamoto, S.; Hijikata, Y.; Zhang, Z.; Awaga, K.; Pirillo, J.; Hijikata, Y.; Awaga, K., Nanopore-Induced Host-Guest Charge Transfer Phenomena in a Metal-Organic Framework. *Chem Sci* **2018,** *9* (13), 3282-3289.

43. Huo, P.; Chen, T.; Hou, J.-L.; Yu, L.; Zhu, Q.-Y.; Dai, J., Ligand-to-Ligand Charge Transfer within Metal–Organic Frameworks Based on Manganese Coordination Polymers with Tetrathiafulvalene-Bicarboxylate and Bipyridine Ligands. *Inorg. Chem.* **2016,** *55* (13), 6496-6503.

44. Wang, J.-L.; Wang, C.; Lin, W., Metal-Organic Frameworks for Light Harvesting and Photocatalysis. *ACS Catal.* **2012,** *2* (12), 2630-2640.

45. Deng, X.; Albero, J.; Xu, L.; Garcia, H.; Li, Z., Construction of a Stable Ru-Re Hybrid System Based on Multifunctional MOF-253 for Efficient Photocatalytic CO_2 Reduction. *Inorg. Chem.* **2018,** *57* (14), 8276-8286.

46. Yang, S.; Fan, D.; Hu, W.; Pattengale, B.; Liu, C.; Zhang, X.; Huang, J., Elucidating Charge Separation Dynamics in a Hybrid Metal-Organic Framework Photocatalyst for Light-Driven H_2 Evolution. *J. Phys. Chem. C* **2018,** *122* (6), 3305-3311.

47. Kong, X.-J.; Lin, Z.; Zhang, Z.-M.; Zhang, T.; Lin, W., Hierarchical Integration of Photosensitizing Metal-Organic Frameworks and Nickel-Containing Polyoxometalates for Efficient Visible-Light-Driven Hydrogen Evolution. *Angew. Chem. Int. Ed.* **2016,** *55* (22), 6411-6416.

48. Chen, Y.-Z.; Wang, Z. U.; Wang, H.; Lu, J.; Yu, S.-H.; Jiang, H.-L., Singlet Oxygen-Engaged Selective Photo-Oxidation over Pt Nanocrystals/Porphyrinic MOF: The Roles of Photothermal Effect and Pt Electronic State. *J. Am. Chem. Soc.* **2017,** *139* (5), 2035-2044.

49. Kung, C.-W.; Otake, K.; Buru, C. T.; Goswami, S.; Cui, Y.; Hupp, J. T.; Spokoyny, A. M.; Farha, O. K., Increased Electrical Conductivity in a Mesoporous Metal–Organic Framework Featuring Metallacarboranes Guests. *J. Am. Chem. Soc.* **2018,** *140* (11), 3871-3875.

50. Xu, H.-Q.; Yang, S.; Ma, X.; Huang, J.; Jiang, H.-L., Unveiling Charge-Separation Dynamics in CdS/Metal–Organic Framework Composites for Enhanced Photocatalysis. *ACS Catal.* **2018,** *8* (12), 11615-11621.

51. Dolgopolova, E. A.; Rice, A. M.; Martin, C. R.; Shustova, N. B., Photochemistry and Photophysics of Mofs: Steps Towards MOF-Based Sensing Enhancements. *Chem. Soc. Rev.* **2018,** *47* (13), 4710-4728.

52. Kuyuldar, S.; Genna, D. T.; Burda, C., On the Potential for Nanoscale Metal–Organic Frameworks for Energy Applications. *J. Mater. Chem. A* **2019,** *7* (38), 21545-21576.

53. Lin, S.; Usov, P. M.; Morris, A. J., The Role of Redox Hopping in Metal–Organic Framework Electrocatalysis. *Chem. Commun.* **2018,** *54* (51), 6965-6974.

54. Liu, W.; Yin, X.-B., Metal–Organic Frameworks for Electrochemical Applications. *TrAC, Trends Anal. Chem.* **2016,** *75*, 86-96.

55. Sariciftci, N. S.; Smilowitz, L.; Heeger, A. J.; Wudl, F., Photoinduced Electron Transfer from a Conducting Polymer to Buckminsterfullerene. *Science* **1992,** *258* (5087), 1474-1476.

56. Yu, J.; Van, W. A.; Deria, P.; Park, J.; Rumbles, G.; Rumbles, G., Excited-State Electronic Properties in Zr-Based Metal-Organic Frameworks as a Function of a Topological Network. *J. Am. Chem. Soc.* **2018,** *140* (33), 10488-10496.

57. Deria, P.; Yu, J.; Smith, T.; Balaraman, R. P., Ground-State Versus Excited-State Interchromophoric Interaction: Topology Dependent Excimer Contribution in Metal–Organic Framework Photophysics. *J. Am. Chem. Soc.* **2017,** *139* (16), 5973-5983.

58. Kent, C. A.; Liu, D.; Ma, L.; Papanikolas, J. M.; Meyer, T. J.; Lin, W., Light Harvesting in Microscale Metal–Organic Frameworks by Energy Migration and Interfacial Electron Transfer Quenching. *J. Am. Chem. Soc.* **2011,** *133* (33), 12940-12943.

59. Son, H.-J.; Jin, S.; Patwardhan, S.; Wezenberg, S. J.; Jeong, N. C.; So, M.; Wilmer, C. E.; Sarjeant, A. A.; Schatz, G. C.; Snurr, R. Q.; Farha, O. K.; Wiederrecht, G. P.; Hupp, J. T., Light-Harvesting and Ultrafast Energy Migration in Porphyrin-Based Metal–Organic Frameworks. *J. Am. Chem. Soc.* **2013,** *135* (2), 862-869.

60. Goswami, S.; Ma, L.; Martinson, A. B. F.; Wasielewski, M. R.; Farha, O. K.; Hupp, J. T., Toward Metal–Organic Framework-Based Solar Cells: Enhancing Directional Exciton Transport by Collapsing Three-Dimensional Film Structures. *ACS Appl. Mater. Interfaces* **2016,** *8* (45), 30863-30870.

61. Marcus, R. A.; Sutin, N., Electron Transfers in Chemistry and Biology. *Biochim. Biophys. Acta, Rev. Bioenerg.* **1985,** *811* (3), 265-322.

62. Weaver, M. J., Correlations between Electrochemical and Homogeneous Redox Reactivity. Quantitative Comparisons of Rate Constants and Activation Parameters for Some Inorganic Outer-Sphere Reactions. *J. Phys. Chem.* **1980,** *84* (6), 568-576.

63. Savéant, J.-M.; Tessier, D., Variation of the Electrochemical Transfer Coefficient with Potential. *Faraday Discuss. Chem. Soc.* **1982,** *74* (0), 57-72.

64. Wherland, S.; Pecht, I., Protein-Protein Electron Transfer. A Marcus Theory Analysis of Reactions between C Type Cytochromes and Blue Copper Proteins. *Biochemistry* **1978,** *17* (13), 2585-2591.

65. Khopde, S. M.; Priyadarsini, K. I., Application of Marcus Theory of Electron Transfer for the Reactions between Hrp Compound I and II and 2,4-Disubstituted Phenols. *Biophys. Chem.* **2000,** *88* (1), 103-109.

66. Candeias, L. P.; Folkes, L. K.; Wardman, P., Factors Controlling the Substrate Specificity of Peroxidases: Kinetics and Thermodynamics of the Reaction of Horseradish Peroxidase Compound I with Phenols and Indole-3-Acetic Acids. *Biochemistry* **1997,** *36* (23), 7081-7085.

67. Jia, Y.; DiMagno, T. J.; Chan, C. K.; Wang, Z.; Popov, M. S.; Du, M.; Hanson, D. K.; Schiffer, M.; Norris, J. R.; Fleming, G. R., Primary Charge Separation in Mutant Reaction Centers of Rhodobacter Capsulatus. *J. Phys. Chem.* **1993,** *97* (50), 13180-13191.

68. Renger, G., Mechanism of Light Induced Water Splitting in Photosystem II of Oxygen Evolving Photosynthetic Organisms. *Biochim. Biophys. Acta, Bioenerg.* **2012,** *1817* (8), 1164-1176.

69. Marcus, R. A., Chemical and Electrochemical Electron-Transfer Theory. **1964,** *15* (1), 155-196.

70. Marcus, R. A., Electron Transfer Reactions in Chemistry. Theory and Experiment. *Rev. Mod. Phys.* **1993,** *65* (3), 599-610.

71. Patwardhan, S.; Schatz, G. C., Theoretical Investigation of Charge Transfer in Metal Organic Frameworks for Electrochemical Device Applications. *J. Phys. Chem. C* **2015,** *119* (43), 24238-24247.

72. Li, X.; Maindan, K.; Deria, P., Metal-Organic Frameworks-Based Electrocatalysis: Insight and Future Perspectives. *Comments Inorg. Chem.* **2018,** *38* (5), 166-209.

73. Rehm, D.; Weller, A., Kinetics of Fluorescence Quenching by Electron and H-Atom Transfer. *Isr. J. Chem.* **1970,** *8* (2), 259-271.

74. Albert, W., Photoinduced Electron Transfer in Solution: Exciplex and Radical Ion Pair Formation Free Enthalpies and Their Solvent Dependence. *Z. Phys. Chem.* **1982,** *133* (1), 93-98.

75. Sarangi, R.; Cho, J.; Nam, W.; Solomon, E. I., XAS and DFT Investigation of Mononuclear Cobalt(III) Peroxo Complexes: Electronic Control of the Geometric Structure in CoO_2 Versus NiO_2 Systems. *Inorg. Chem.* **2011,** *50* (2), 614-620.

76. Canton, S. E.; Zhang, X.; Zhang, J.; van Driel, T. B.; Kjaer, K. S.; Haldrup, K.; Chabera, P.; Harlang, T.; Suarez-Alcantara, K.; Liu, Y.; Pérez, J.; Bordage, A.; Pápai, M.; Vankó, G.; Jennings, G.; Kurtz, C. A.; Rovezzi, M.; Glatzel, P.; Smolentsev, G.; Uhlig, J.; Dohn, A. O.; Christensen, M.; Galler, A.; Gawelda, W.; Bressler, C.; Lemke, H. T.; Møller, K. B.; Nielsen, M. M.; Lomoth, R.; Wärnmark, K.; Sundström, V., Toward Highlighting the Ultrafast Electron Transfer Dynamics at the Optically Dark Sites of Photocatalysts. *J. Phys. Chem. Lett.* **2013,** *4* (11), 1972-1976.

77. Hanna, L.; Kucheryavy, P.; Liu, C.; Zhang, X.; Lockard, J. V., Long-Lived Photoinduced Charge Separation in a Trinuclear Iron-M_3-Oxo-Based Metal-Organic Framework. *J. Phys. Chem. C* **2017,** *121* (25), 13570-13576.

78. Hendon, C. H.; Tiana, D.; Fontecave, M.; Sanchez, C.; D'arras, L.; Sassoye, C.; Rozes, L.; Mellot-Draznieks, C.; Walsh, A., Engineering the Optical Response of the Titanium-Mil-125 Metal–Organic Framework through Ligand Functionalization. *J. Am. Chem. Soc.* **2013,** *135* (30), 10942-10945.

79. Santaclara, J. G.; Olivos-Suarez, A. I.; Gonzalez-Nelson, A.; Osadchii, D.; Nasalevich, M. A.; van der Veen, M. A.; Kapteijn, F.; Sheveleva, A. M.; Veber, S. L.; Fedin, M. V.; Murray, A. T.; Hendon, C. H.; Walsh, A.; Gascon, J., Revisiting the Incorporation of Ti(IV) in UiO-Type Metal–Organic Frameworks: Metal Exchange Versus Grafting and Their Implications on Photocatalysis. *Chem. Mater.* **2017,** *29* (21), 8963-8967.

80. Horiuchi, Y.; Toyao, T.; Saito, M.; Mochizuki, K.; Iwata, M.; Higashimura, H.; Anpo, M.; Matsuoka, M., Visible-Light-Promoted Photocatalytic Hydrogen Production by Using an Amino-Functionalized Ti(IV) Metal–Organic Framework. *J. Phys. Chem. C* **2012,** *116* (39), 20848-20853.

81. Santiago Portillo, A.; Baldovi, H. G.; Garcia Fernandez, M. T.; Navalon, S.; Atienzar, P.; Ferrer, B.; Alvaro, M.; Garcia, H.; Li, Z., Ti as Mediator in the Photoinduced Electron Transfer of Mixed-Metal NH_2-UiO-66(Zr/Ti): Transient Absorption Spectroscopy Study and Application in Photovoltaic Cell. *J. Phys. Chem. C* **2017,** *121* (12), 7015-7024.

82. Nasalevich, M. A.; Hendon, C. H.; Santaclara, J. G.; Svane, K.; van der Linden, B.; Veber, S. L.; Fedin, M. V.; Houtepen, A. J.; van der Veen, M. A.; Kapteijn, F.; Walsh, A.; Gascon, J., Electronic Origins of Photocatalytic Activity in D0 Metal Organic Frameworks. *Sci. Rep.* **2016,** *6* (1), 23676.

83. Padial, N. M.; Castells-Gil, J.; Almora-Barrios, N.; Romero-Angel, M.; da Silva, I.; Barawi, M.; García-Sánchez, A.; de la Peña O'Shea, V. A.; Martí-Gastaldo, C., Hydroxamate Titanium–Organic Frameworks and the Effect of Siderophore-Type Linkers over Their

Photocatalytic Activity. *J. Am. Chem. Soc.* **2019,** *141* (33), 13124-13133.

84. Castells-Gil, J.; Padial, N. M.; Almora-Barrios, N.; Albero, J.; Ruiz-Salvador, A. R.; González-Platas, J.; García, H.; Martí-Gastaldo, C., Chemical Engineering of Photoactivity in Heterometallic Titanium–Organic Frameworks by Metal Doping. *Angew. Chem. Int. Ed.* **2018,** *57* (28), 8453-8457.

85. Goswami, S.; Ray, D.; Otake, K.-i.; Kung, C.-W.; Garibay, S. J.; Islamoglu, T.; Atilgan, A.; Cui, Y.; Cramer, C. J.; Farha, O. K.; Hupp, J. T., A Porous, Electrically Conductive Hexa-Zirconium(IV) Metal–Organic Framework. *Chem. Sci.* **2018,** *9* (19), 4477-4482.

86. Williams, D. E.; Dolgopolova, E. A.; Godfrey, D. C.; Ermolaeva, E. D.; Pellechia, P. J.; Greytak, A. B.; Smith, M. D.; Avdoshenko, S. M.; Popov, A. A.; Shustova, N. B., Fulleretic Well-Defined Scaffolds: Donor–Fullerene Alignment through Metal Coordination and Its Effect on Photophysics. *Angew. Chem. Int. Ed.* **2016,** *55* (31), 9070-9074.

87. Wu, X.-P.; Gagliardi, L.; Truhlar, D. G., Cerium Metal–Organic Framework for Photocatalysis. *J. Am. Chem. Soc.* **2018**, 140 (25), 7904-7912

88. Li, P.; Chen, Q.; Wang, T. C.; Vermeulen, N. A.; Mehdi, B. L.; Dohnalkova, A.; Browning, N. D.; Shen, D.; Anderson, R.; Gómez-Gualdrón, D. A.; Cetin, F. M.; Jagiello, J.; Asiri, A. M.; Stoddart, J. F.; Farha, O. K., Hierarchically Engineered Mesoporous Metal-Organic Frameworks toward Cell-Free Immobilized Enzyme Systems. *Chem* **2018,** *4* (5), 1022-1034.

89. Lyu, J.; Zhang, X.; Otake, K.-i.; Wang, X.; Li, P.; Li, Z.; Chen, Z.; Zhang, Y.; Wasson, M. C.; Yang, Y.; Bai, P.; Guo, X.; Islamoglu, T.; Farha, O. K., Topology and Porosity Control of Metal–Organic Frameworks through Linker Functionalization. *Chem. Sci.* **2019,** *10* (4), 1186-1192.

90. Chen, Z.; Hanna, S. L.; Redfern, L. R.; Alezi, D.; Islamoglu, T.; Farha, O. K., Reticular Chemistry in the Rational Synthesis of Functional Zirconium Cluster-Based Mofs. *Coord. Chem. Rev.* **2019,** *386*, 32-49.

91. Yuan, S.; Huang, L.; Huang, Z.; Sun, D.; Qin, J.-S.; Feng, L.; Li, J.; Zou, X.; Cagin, T.; Zhou, H.-C., Continuous Variation of Lattice Dimensions and Pore Sizes in Metal–Organic Frameworks. *J. Am. Chem. Soc.* **2020,** *142* (10), 4732-4738.

92. Kung, C.-W.; Wang, T. C.; Mondloch, J. E.; Fairen-Jimenez, D.; Gardner, D. M.; Bury, W.; Klingsporn, J. M.; Barnes, J. C.; Van Duyne, R.; Stoddart, J. F.; Wasielewski, M. R.; Farha, O. K.; Hupp, J. T., Metal–Organic Framework Thin Films Composed of Free-Standing Acicular Nanorods Exhibiting Reversible Electrochromism. *Chem. Mater.* **2013,** *25* (24), 5012-5017.

93. Deria, P.; Gómez-Gualdrón, D. A.; Hod, I.; Snurr, R. Q.; Hupp, J. T.; Farha, O. K., Framework-Topology-Dependent Catalytic Activity of Zirconium-Based (Porphinato)Zinc(II) MOFs. *J. Am. Chem. Soc.* **2016,** *138* (43), 14449-14457.

94. Islamoglu, T.; Goswami, S.; Li, Z.; Howarth, A. J.; Farha, O. K.; Hupp, J. T., Postsynthetic Tuning of Metal–Organic Frameworks for Targeted Applications. *Acc. Chem. Res.* **2017,** *50* (4), 805-813.

95. Van Wyk, A.; Smith, T.; Park, J.; Deria, P., Charge-Transfer within Zr-Based Metal-Organic Framework: The Role of Polar Node. *J. Am. Chem. Soc.* **2018,** *140* (8), 2756-2760.

96. Celis-Salazar, P. J.; Cai, M.; Cucinell, C. A.; Ahrenholtz, S. R.; Epley, C. C.; Usov, P. M.; Morris, A. J., Independent Quantification of Electron and Ion Diffusion in Metallocene-Doped Metal–Organic Frameworks Thin Films. *J. Am. Chem. Soc.* **2019,** *141* (30), 11947-11953.

97. Oisaki, K.; Li, Q.; Furukawa, H.; Czaja, A. U.; Yaghi, O. M., A Metal–Organic Framework with Covalently Bound Organometallic Complexes. *J. Am. Chem. Soc.* **2010,** *132* (27), 9262-9264.

98. Feng, X.; Song, Y.; Li, Z.; Kaufmann, M.; Pi, Y.; Chen, J. S.; Xu, Z.; Li, Z.; Wang, C.; Lin, W., Metal–Organic Framework Stabilizes a Low-Coordinate Iridium Complex for Catalytic Methane Borylation. *J. Am. Chem. Soc.* **2019,** *141* (28), 11196-11203.

99. Fang, Y.; Xiao, Z.; Kirchon, A.; Li, J.; Jin, F.; Togo, T.; Zhang, L.; Zhu, C.; Zhou, H.-C., Bimolecular Proximity of a Ruthenium Complex and Methylene Blue within an Anionic Porous Coordination Cage for Enhancing Photocatalytic Activity. *Chem. Sci.* **2019,** *10* (12), 3529-3534.

100. Liu, J.; Redfern, L. R.; Liao, Y.; Islamoglu, T.; Atilgan, A.; Farha, O. K.; Hupp, J. T., Metal–Organic-Framework-Supported and -Isolated Ceria Clusters with Mixed Oxidation States. *ACS Appl. Mater. Interfaces* **2019,** *11* (51), 47822-47829.

101. Noh, H.; Kung, C.-W.; Otake, K.-i.; Peters, A. W.; Li, Z.; Liao, Y.; Gong, X.; Farha, O. K.; Hupp, J. T., Redox-Mediator-Assisted Electrocatalytic Hydrogen Evolution from Water by a Molybdenum Sulfide-Functionalized Metal–Organic Framework. *ACS Catal.* **2018,** *8* (10), 9848-9858.

102. Ahn, S.; Nauert, S. L.; Buru, C. T.; Rimoldi, M.; Choi, H.; Schweitzer, N. M.; Hupp, J. T.; Farha, O. K.; Notestein, J. M., Pushing the Limits on Metal–Organic Frameworks as a Catalyst Support: NU-1000 Supported Tungsten Catalysts for o-Xylene Isomerization and Disproportionation. *J. Am. Chem. Soc.* **2018,** *140* (27), 8535-8543.

103. Choi, H.; Peters, A. W.; Noh, H.; Gallington, L. C.; Platero-Prats, A. E.; DeStefano, M. R.; Rimoldi, M.; Goswami, S.; Chapman, K. W.; Farha, O. K.; Hupp, J. T., Vapor-Phase Fabrication and Condensed-Phase Application of a MOF-Node-Supported Iron Thiolate Photocatalyst for Nitrate Conversion to Ammonium. *ACS Appl. Energy Mater.* **2019,** *2* (12), 8695-8700.

104. Majewski, M. B.; Howarth, A. J.; Li, P.; Wasielewski, M. R.; Hupp, J. T.; Farha, O. K., Enzyme Encapsulation in Metal–Organic Frameworks for Applications in Catalysis. *Cryst. Eng. Comm.* **2017,** *19* (29), 4082-4091.

105. Pan, Y.; Li, H.; Farmakes, J.; Xiao, F.; Chen, B.; Ma, S.; Yang, Z., How Do Enzymes Orient When Trapped on Metal–Organic Framework (MOF) Surfaces? *J. Am. Chem. Soc.* **2018,** *140* (47), 16032-16036.

106. Gkaniatsou, E.; Sicard, C.; Ricoux, R.; Mahy, J.-P.; Steunou, N.; Serre, C., Metal–Organic Frameworks: A Novel Host Platform for Enzymatic Catalysis and Detection. *Mater. Horiz.* **2017,** *4* (1), 55-63.

107. Li, X.; Yu, J.; Gosztola, D. J.; Fry, H. C.; Deria, P., Wavelength-Dependent Energy and Charge Transfer in Mof: A Step toward Artificial Porous Light-Harvesting System. *J. Am. Chem. Soc.* **2019,** *141* (42), 16849-16857.

108. Baek, J.; Rungtaweevoranit, B.; Pei, X.; Park, M.; Fakra, S. C.; Liu, Y.-S.; Matheu, R.; Alshmimri, S. A.; Alshehri, S.; Trickett, C. A.; Somorjai, G. A.; Yaghi, O. M., Bioinspired Metal–Organic Framework Catalysts for Selective Methane Oxidation to Methanol. *J. Am. Chem. Soc.* **2018,** *140* (51), 18208-18216.

109. Taddei, M.; Wakeham, R. J.; Koutsianos, A.; Andreoli, E.; Barron, A. R., Post-Synthetic Ligand Exchange in Zirconium-Based Metal–Organic Frameworks: Beware of the Defects! *Angew. Chem. Int. Ed.* **2018,** *57* (36), 11706-11710.

110. Liberman, I.; Shimoni, R.; Ifraemov, R.; Rozenberg, I.; Singh, C.; Hod, I., Active-Site Modulation in an Fe-Porphyrin-Based Metal–Organic Framework through Ligand Axial Coordination: Accelerating Electrocatalysis and Charge-Transport Kinetics. *J. Am. Chem. Soc.* **2020,** *142* (4), 1933-1940.

111.   Deria, P.; Bury, W.; Hod, I.; Kung, C.-W.; Karagiaridi, O.; Hupp, J. T.; Farha, O. K., Mof Functionalization Via Solvent-Assisted Ligand Incorporation: Phosphonates Vs Carboxylates. *Inorg. Chem.* **2015,** *54* (5), 2185-2192.

112.   Hod, I.; Bury, W.; Gardner, D. M.; Deria, P.; Roznyatovskiy, V.; Wasielewski, M. R.; Farha, O. K.; Hupp, J. T., Bias-Switchable Permselectivity and Redox Catalytic Activity of a Ferrocene-Functionalized, Thin-Film Metal–Organic Framework Compound. *J. Phys. Chem. Lett.* **2015,** *6*, 586-591.

113.   Hod, I.; Farha, O. K.; Hupp, J. T., Modulating the Rate of Charge Transport in a Metal–Organic Framework Thin Film Using Host: Guest Chemistry. *Chem. Commun.* **2016,** *52*, 1705-1708.

114.   Patwardhan, S.; Schatz, G. C., Theoretical Investigation of Charge Transfer in Metal Organic Frameworks for Electrochemical Device Applications. *J. Phys. Chem. C* **2015,** *119*, 24238-24247.

115.   McKeithan, C. R.; Wojtas, L.; Larsen, R. W., Guest to Framework Photoinduced Electron Transfer in a Cobalt Substituted Rwlc-2 Metal Organic Framework. *Dalton Trans.* **2018,** *47* (28), 9250-9256.

116.   Larsen, R. W.; Wojtas, L., Fixed Distance Photoinduced Electron Transfer between Fe and Zn Porphyrins Encapsulated within the Zn HKUST-1 Metal Organic Framework. *Dalton Trans.* **2015,** *44* (7), 2959-2963.

117.   Pratik, S. M.; Gagliardi, L.; Cramer, C. J., Boosting Photoelectric Conductivity in Porphyrin-Based Mofs Incorporating C60. *J. Phys. Chem. C* **2020,** *124* (3), 1878-1887.

118.   Ravelli, D.; Dondi, D.; Fagnoni, M.; Albini, A., Photocatalysis. A Multi-Faceted Concept for Green Chemistry. *Chem. Soc. Rev.* **2009,** *38* (7), 1999-2011.

119.   Meng, A.-N.; Chaihu, L.-X.; Chen, H.-H.; Gu, Z.-Y., Ultrahigh Adsorption and Singlet-Oxygen Mediated Degradation for Efficient Synergetic Removal of Bisphenol a by a Stable Zirconium-Porphyrin Metal-Organic Framework. *Sci. Rep.* **2017,** *7* (1), 6297.

120.   Park, J.; Jiang, Q.; Feng, D.; Zhou, H.-C., Controlled Generation of Singlet Oxygen in Living Cells with Tunable Ratios of the Photochromic Switch in Metal–Organic Frameworks. *Angew. Chem. Int. Ed.* **2016,** *55* (25), 7188-7193.

121.   Atilgan, A.; Islamoglu, T.; Howarth, A. J.; Hupp, J. T.; Farha, O. K., Detoxification of a Sulfur Mustard Simulant Using a Bodipy-Functionalized Zirconium-Based Metal–Organic Framework. *ACS Appl. Mater. Interfaces* **2017,** *9* (29), 24555-24560.

122.   Goswami, S.; Miller, C. E.; Logsdon, J. L.; Buru, C. T.; Wu, Y.-L.; Bowman, D. N.; Islamoglu, T.; Asiri, A. M.; Cramer, C. J.; Wasielewski, M. R.; Hupp, J. T.; Farha, O. K., Atomistic Approach toward Selective Photocatalytic Oxidation of a Mustard-Gas Simulant: A Case Study with Heavy-Chalcogen-Containing PCN-57 Analogues. *ACS Appl. Mater. Interfaces* **2017,** *9* (23), 19535-19540.

123.   Fang, W.-H.; Zhang, L.; Zhang, J., A 3.6 nm Ti$_{52}$–Oxo Nanocluster with Precise Atomic Structure. *J. Am. Chem. Soc.* **2016,** *138* (24), 7480-7483.

124.   Hong, Z.-F.; Xu, S.-H.; Yan, Z.-H.; Lu, D.-F.; Kong, X.-J.; Long, L.-S.; Zheng, L.-S., A Large Titanium Oxo Cluster Featuring a Well-Defined Structural Unit of Rutile. *Cryst. Growth. Des.* **2018,** *18* (9), 4864-4868.

125.   Song, Y.; Li, Z.; Zhu, Y.; Feng, X.; Chen, J. S.; Kaufmann, M.; Wang, C.; Lin, W., Titanium Hydroxide Secondary Building Units in Metal-Organic Frameworks Catalyze Hydrogen Evolution under Visible Light. *J. Am. Chem. Soc.* **2019,** *141* (31), 12219-12223.

126.   Yan, Z.-H.; Du, M.-H.; Liu, J.; Jin, S.; Wang, C.; Zhuang, G.-L.; Kong, X.-J.; Long, L.-S.; Zheng, L.-S., Photo-Generated Dinuclear {Eu(II)}2 Active Sites for Selective CO$_2$ Reduction in a Photosensitizing Metal-Organic Framework. *Nat. Commun.* **2018,** *9* (1), 1-9.

127.   Goldsmith, J. I.; Hudson, W. R.; Lowry, M. S.; Anderson, T. H.; Bernhard, S., Discovery and High-Throughput Screening of Heteroleptic Iridium Complexes for Photoinduced Hydrogen Production. *J. Am. Chem. Soc.* **2005,** *127* (20), 7502-7510.

128.   Nagib, D. A.; Scott, M. E.; MacMillan, D. W. C., Enantioselective A-Trifluoromethylation of Aldehydes Via Photoredox Organocatalysis. *J. Am. Chem. Soc.* **2009,** *131* (31), 10875-10877.

129.   Condie, A. G.; González-Gómez, J. C.; Stephenson, C. R. J., Visible-Light Photoredox Catalysis: Aza-Henry Reactions Via C–H Functionalization. *J. Am. Chem. Soc.* **2010,** *132* (5), 1464-1465.

130.   Flamigni, L.; Barbieri, A.; Sabatini, C.; Ventura, B.; Barigelletti, F., Photochemistry and Photophysics of Coordination Compounds: Iridium. In *Photochemistry and Photophysics of Coordination Compounds Ii*, Balzani, V.; Campagna, S., Eds. Springer Berlin Heidelberg: Berlin, Heidelberg, 2007; pp 143-203.

131.   Pellegrin, Y.; Odobel, F., Sacrificial Electron Donor Reagents for Solar Fuel Production. *C. R. Chim.* **2017,** *20* (3), 283-295.

132.   Kalyanasundaram, K.; Kiwi, J.; Grätzel, M., Hydrogen Evolution from Water by Visible Light, a Homogeneous Three Component Test System for Redox Catalysis. *Helv. Chim. Acta.* **1978,** *61* (7), 2720-2730.

133.   Manke, A.-M.; Geisel, K.; Fetzer, A.; Kurz, P., A Water-Soluble Tin(Iv) Porphyrin as a Bioinspired Photosensitiser for Light-Driven Proton-Reduction. *Phys. Chem. Chem. Phys.* **2014,** *16* (24), 12029-12042.

134.   Lan, G.; Li, Z.; Veroneau, S. S.; Zhu, Y.-Y.; Xu, Z.; Wang, C.; Lin, W., Photosensitizing Metal-Organic Layers for Efficient Sunlight-Driven Carbon Dioxide Reduction. *J. Am. Chem. Soc.* **2018,** *140* (39), 12369-12373.

135.   Sampaio, R. N.; Grills, D. C.; Polyansky, D. E.; Szalda, D. J.; Fujita, E., Unexpected Roles of Triethanolamine in the Photochemical Reduction of CO$_2$ to Formate by Ruthenium Complexes. *J. Am. Chem. Soc.* **2020,** *142* (5), 2413-2428.

136.   Ishida, H.; Tanaka, K.; Tanaka, T., Electrochemical CO$_2$ Reduction Catalyzed by Ruthenium Complexes [Ru(Bpy)2(CO)$_2$]$^{2+}$ and [Ru(Bpy)$_2$(CO)Cl]$^+$. Effect of Ph on the Formation of Co and Hcoo. *Organometallics* **1987,** *6* (1), 181-186.

137.   Tamaki, Y.; Morimoto, T.; Koike, K.; Ishitani, O., Photocatalytic Co2 Reduction with High Turnover Frequency and Selectivity of Formic Acid Formation Using Ru(II) Multinuclear Complexes. *Proc. Natl. Acad. Sci. U.S.A* **2012,** *109* (39), 15673-15678.

138.   Hasegawa, E.; Takizawa, S.; Seida, T.; Yamaguchi, A.; Yamaguchi, N.; Chiba, N.; Takahashi, T.; Ikeda, H.; Akiyama, K., Photoinduced Electron-Transfer Systems Consisting of Electron-Donating Pyrenes or Anthracenes and Benzimidazolines for Reductive Transformation of Carbonyl Compounds. *Tetrahedron* **2006,** *62* (27), 6581-6588.

139.   Xia, Z.; He, C.; Wang, X.; Duan, C., Modifying Electron Transfer between Photoredox and Organocatalytic Units Via Framework Interpenetration for B-Carbonyl Functionalization. *Nat. Commun.* **2017,** *8* (1), 1-11.

140.   Hod, I.; Farha, O. K.; Hupp, J. T., Modulating the Rate of Charge Transport in a Metal-Organic Framework Thin Film Using Host:Guest Chemistry. *Chem. Commun.* **2016,** *52* (8), 1705-1708.

141.   Maindan, K.; Li, X.; Yu, J.; Deria, P. J. T. J. o. P. C. B., Controlling Charge-Transport in Metal-Organic Frameworks: Contribution of Topological and Spin-State Variation on the Fe-Porphyrin Centered Redox Hopping Rate. *J. Phys. Chem. B* **2019**.

142.   Sun, L.; Campbell, M. G.; Dincă, M., Electrically Conductive Porous Metal–Organic Frameworks. *Angew. Chem. Int. Ed.* **2016,** *55* (11), 3566-3579.

143. Kung, C.-W.; Goswami, S.; Hod, I.; Wang, T. C.; Duan, J.; Farha, O. K.; Hupp, J. T., Charge Transport in Zirconium-Based Metal–Organic Frameworks. *Acc. Chem. Res.* **2020**.

144. Natarajan, K.; Gupta, A. K.; Ansari, S. N.; Saraf, M.; Mobin, S. M., Mixed-Ligand-Architected 2d Co(Ii)-Mof Expressing a Novel Topology for an Efficient Photoanode for Water Oxidation Using Visible Light. *ACS Appl. Mater. Interfaces* **2019,** *11* (14), 13295-13303.

145. Zhang, C.; Li, X.; Kang, S.-z.; Qin, L.; Li, G.; Mu, J., Photoelectronically Active, Metal Organic Framework Films Prepared by Self-Directed Assembly of Silanized Porphyrin Cobalt Monomers. *Chem. Commun.* **2014,** *50* (65), 9064-9067.

146. Zhang, W.; Li, R.; Zhao, X.; Chen, Z.; Law, A. W.-K.; Zhou, K., A Cobalt-Based Metal-Organic Framework as Cocatalyst on Bivo4 Photoanode for Enhanced Photoelectrochemical Water Oxidation. *ChemSusChem* **2018,** *11* (16), 2710-2716.

147. Downes, C. A.; Marinescu, S. C., Efficient Electrochemical and Photoelectrochemical H2 Production from Water by a Cobalt Dithiolene One-Dimensional Metal-Organic Surface. *J. Am. Chem. Soc.* **2015,** *137* (43), 13740-13743.

148. Bard, A. J., Photoelectrochemistry. **1980,** *207* (4427), 139-144.

149. Garcia-Sanchez, A.; Gomez-Mendoza, M.; Barawi, M.; Villar-Garcia, I. J.; Liras, M.; Gandara, F.; de la Pena O'Shea, V. A., Fundamental Insights into Photoelectrocatalytic Hydrogen Production with a Hole-Transport Bismuth Metal-Organic Framework. *J. Am. Chem. Soc.* **2020,** *142* (1), 318-326.

150. Lin, S.; Cairnie, D. R.; Davis, D.; Chakraborty, A.; Cai, M.; Morris, A. J., Photoelectrochemical Alcohol Oxidation by Mixed-Linker Metal-Organic Frameworks. *Faraday Discuss.* **2020**.

151. Zhou, S.; Yue, P.; Huang, J.; Wang, L.; She, H.; Wang, Q., High-Performance Photoelectrochemical Water Splitting of BiVO$_4$@Co-Mim Prepared by a Facile in-Situ Deposition Method. *Chem. Eng. J.* **2019,** *371*, 885-892.

152. Cordova Wong, B. J.; Xu, D.-m.; Bao, S.-S.; Zheng, L.-M.; Lei, J., Hofmann Metal-Organic Framework Monolayer Nanosheets as an Axial Coordination Platform for Biosensing. *ACS Appl. Mater. Interfaces* **2019,** *11* (13), 12986-12992.

153. Jurcic, M.; Peveler, W. J.; Savory, C. N.; Bucar, D.-K.; Kenyon, A. J.; Scanlon, D. O.; Parkin, I. P., Sensing and Discrimination of Explosives at Variable Concentrations with a Large-Pore Mof as Part of a Luminescent Array. *ACS Appl. Mater. Interfaces* **2019,** *11* (12), 11618-11626.

154. Masih, D.; Chernikova, V.; Shekhah, O.; Eddaoudi, M.; Mohammed, O. F., Zeolite-Like Metal-Organic Framework (Mof) Encaged Pt(Ii)-Porphyrin for Anion-Selective Sensing. *ACS Appl. Mater. Interfaces* **2018,** *10* (14), 11399-11405.

155. Dong, B.-X.; Pan, Y.-M.; Liu, W.-L.; Teng, Y.-L., An Ultrastable Luminescent Metal-Organic Framework for Selective Sensing of Nitroaromatic Compounds and Nitroimidazole-Based Drug Molecules. *Cryst. Growth. Des.* **2018,** *18* (1), 431-440.

156. Dalapati, R.; Nandi, S.; Reinsch, H.; Bhunia, B. K.; Mandal, B. B.; Stock, N.; Biswas, S., Fluorogenic Naked-Eye Sensing and Live-Cell Imaging of Cyanide by a Hydrazine-Functionalized CAU-10 Metal-Organic Framework. *Cryst. Eng. Comm.* **2018,** *20* (29), 4194-4201.

157. Ning, D.; Liu, Q.; Wang, Q.; Du, X.-M.; Li, Y.; Ruan, W.-J., Pyrene-Based MOFs as Fluorescent Sensors for Pahs: An Energetic Pathway of the Backbone Structure Effect on Response. *Dalton Trans.* **2019,** *48* (17), 5705-5712.

158. Khatun, A.; Panda, D. K.; Saha, S.; Sayresmith, N.; Walter, M. G., Thiazolothiazole-Based Luminescent Metal-Organic Frameworks with Ligand-to-Ligand Energy Transfer and Hg(2+)-Sensing Capabilities. *Inorg. Chem.* **2019,** *58* (19), 12707-12715.

159. Wang, B.; Yang, Q.; Guo, C.; Sun, Y.; Xie, L.-H.; Li, J.-R., Stable Zr(Iv)-Based Metal-Organic Frameworks with Predesigned Functionalized Ligands for Highly Selective Detection of Fe(III) Ions in Water. *ACS Appl. Mater. Interfaces* **2017,** *9* (11), 10286-10295.

160. Yan, B., Lanthanide-Functionalized Metal–Organic Framework Hybrid Systems to Create Multiple Luminescent Centers for Chemical Sensing. *Acc. Chem. Res.* **2017,** *50* (11), 2789-2798.

161. Cui, Y.; Yue, D.; Huang, Y.; Zhang, J.; Wang, Z.; Yang, D.; Qian, G., Photo-Induced Electron Transfer in a Metal-Organic Framework: A New Approach Towards a Highly Sensitive Luminescent Probe for Fe^{3+}. *Chem. Commun.* **2019,** *55* (75), 11231-11234.

162. Gui, B.; Meng, Y.; Xie, Y.; Tian, J.; Yu, G.; Zeng, W.; Zhang, G.; Gong, S.; Yang, C.; Zhang, D.; Wang, C., Tuning the Photoinduced Electron Transfer in a Zr-MOF: Toward Solid-State Fluorescent Molecular Switch and Turn-on Sensor. *Adv. Mater.* **2018,** *30* (34), 1802329.

163. Li, Q.; Wu, X.; Huang, X.; Deng, Y.; Chen, N.; Jiang, D.; Zhao, L.; Lin, Z.; Zhao, Y., Tailoring the Fluorescence of Aie-Active Metal-Organic Frameworks for Aqueous Sensing of Metal Ions. *ACS Appl. Mater. Interfaces* **2018,** *10* (4), 3801-3809.

.

166x102mm (300 x 300 DPI)